1993

Measurements of the Zeeman mixing cross section of (6)(2)P(1/2)Cs atoms, induced by collision with helium gases.

Ju. Gao
University of Windsor

NOTICE

AVIS

Canada

MEASUREMENTS OF THE ZEEMAN MIXING CROSS SECTION OF

$6^2P_{1/2}$ CS ATOMS, INDUCED BY COLLISION WITH HE GASES

by

Ju   Gao

A Thesis
Submitted to the Faculty of Graduate Studies through the
Department of Physics in Partial Fulfillment of
the Requirements for the Degree of
Master of Science at the
University of Windsor

Windsor, Ontario
1993

Canada

Name _____

Dissertation Abstracts International is arranged by broad, general subject categories. Please select the one subject which most nearly describes the content of your dissertation. Enter the corresponding four-digit code in the spaces provided.

SUBJECT TERM   SUBJECT CODE

Subject Categories

THE HUMANITIES AND SOCIAL SCIENCES

THE SCIENCES AND ENGINEERING

⊕

ABSTRACT

Collisional transitions between Zeeman substates of Cs $6^2P_{1/2}$ atoms in collisions with He atoms have been investigated by methods of atomic fluorescence spectroscopy.

Cs vapour contained in a quartz cell together with helium at low pressure, was selectively excited by pulsed dye-laser radiation to the $6^2P_{1/2,-1/2}$ Zeeman substate in a magnetic field of strength ranging from 1.5 T to 7 T. The fluorescence spectrum consisting of components emitted from the directly excited state and from the collisionally populated state, was resolved with a Fabry-Perot interferometer. Measurements of the relative intensities of the fluorescence components yielded the Zeeman mixing cross section for Cs-He collisions. It was found that the enhancement in the cross section varied as B^2 in the range $0 < B < 0.76T$ and followed a $B^{0.45}$ dependence in the range from $0.76T$ to 5 T, where it peaked and declined slightly at $B > 5T$. A theoretical calculation of the magnetic-field enhancement of the cross section was also carried out, using time-dependent perturbation theory. The results of the calculation are in very good agreement with the experimental results at fields in the range $0 < B < 5$ T, though not beyond 5 T where further theoretical work remains to be done.

ACKNOWLEDGEMENTS

TABLE OF CONTENTS

LIST OF TABLES

LIST OF FIGURES

I INTRODUCTION

The orientation and alignment of excited atoms, as well as the collisional relaxation and transfer of atomic multipole moments, have been the subject of several recent experimental investigations. For example, the transfers between the resonance $^2P_{1/2}$ and $^2P_{3/2}$ Zeeman substates in Na were studied by Kimura et al.(1992), in 5^2P K atoms by Berends et al.(1988), and in 6^2P Rb atoms by Kedzierski et al.(1991). The process $^1P_1(m'_J) \rightarrow {}^3P_2(m_J)$ in Ba, induced in collisions with some diatomic molecules, was investigated by Mestdagh et al.(1993), and the alignment-to-orientation conversion in Na by Han and Schinn (1991).

There has also been some interest in exploring the effect of a magnetic field on m_J mixing rates (or cross sections) in Na (Gay and Schneider 1979a) and Hg (Gay and Schneider 1979b) and, more recently, in Ne, where the magnetic-field dependence of collisional disalignment rates was investigated in fields up to 10T (Matsumoto et al. 1991).

In this investigation I report the results of experiments in which we excited one of the two m_J Zeeman substates of $6^2P_{1/2}$ cesium atoms in magnetic fields up to 7T, and followed the transfer of population to the other m_J substate, induced by He collisions. Since both the Cs vapour pressure and the He pressures were kept low, effects due to trapping of resonance radiation were negligible as was the collisional $^2P_{1/2}-^2P_{3/2}$ mixing. The resulting Zeeman fluorescence spectrum, consisting

of just two components, was resolved with a Fabry-Perot interferometer and measurements of the relative intensities yielded the m_J mixing cross section in relation to the magnetic field strength. I also carried out an independent calculation which predicted the variation of the cross section with the field strength and permitted a comparison with the experimental results. This work follows an earlier study of Cs $^2P_{1/2}$ disorientation cross section over a much smaller range of magnetic fields (Guiry and Krause 1975), the results of which are found to match well with those reported here.

II   THEORY

II.1   Collisions of oriented $6^2P_{1/2}$ Cs atoms with
ground-state He atoms in a magnetic field

An explanation for the effect of the magnetic field on
the Cs $6^2P_{1/2}$ Zeeman mixing cross section was proposed by
Baylis (1971), who suggested that magnetic-field-induced
(virtual) $P_{1/2} \rightarrow P_{3/2}$ mixing enhances Zeeman mixing rates. This
model is now explored further using time-dependent
perturbation theory (TDPT). The Hamiltonian describing a
collision process in the presence of a magnetic field may be
written:

$$H = H_0 + \mu_0(2S+L) \cdot B + V(t) \qquad (II.1.1)$$

where H_0 is the Hamiltonian in the absence of the magnetic
field B, and $V(t)$ represents the collisional interaction
between Cs and He atoms. L and S are the orbit and spin
angular momenta respectively, and μ_0 is the Bohr magneton of
the electron. The magnetic field B was assumed sufficiently
weak to be treated as a perturbation, but sufficiently strong
that it was not necessary to consider hyperfine-structure. A
calculation justifying this assumption appears in Appendix A.

Omitting the collisional interaction, eq.(II.1.1)
becomes:

$$H_B = H_0 + \mu_0(2S+L) \cdot B \qquad (II.1.2)$$

where H_B is the Hamiltonian without the collisional
interaction. By perturbation theory, the eigenstates of H_B

Figure 1. The Grotrian diagram for the Cs atom.

Cs

5
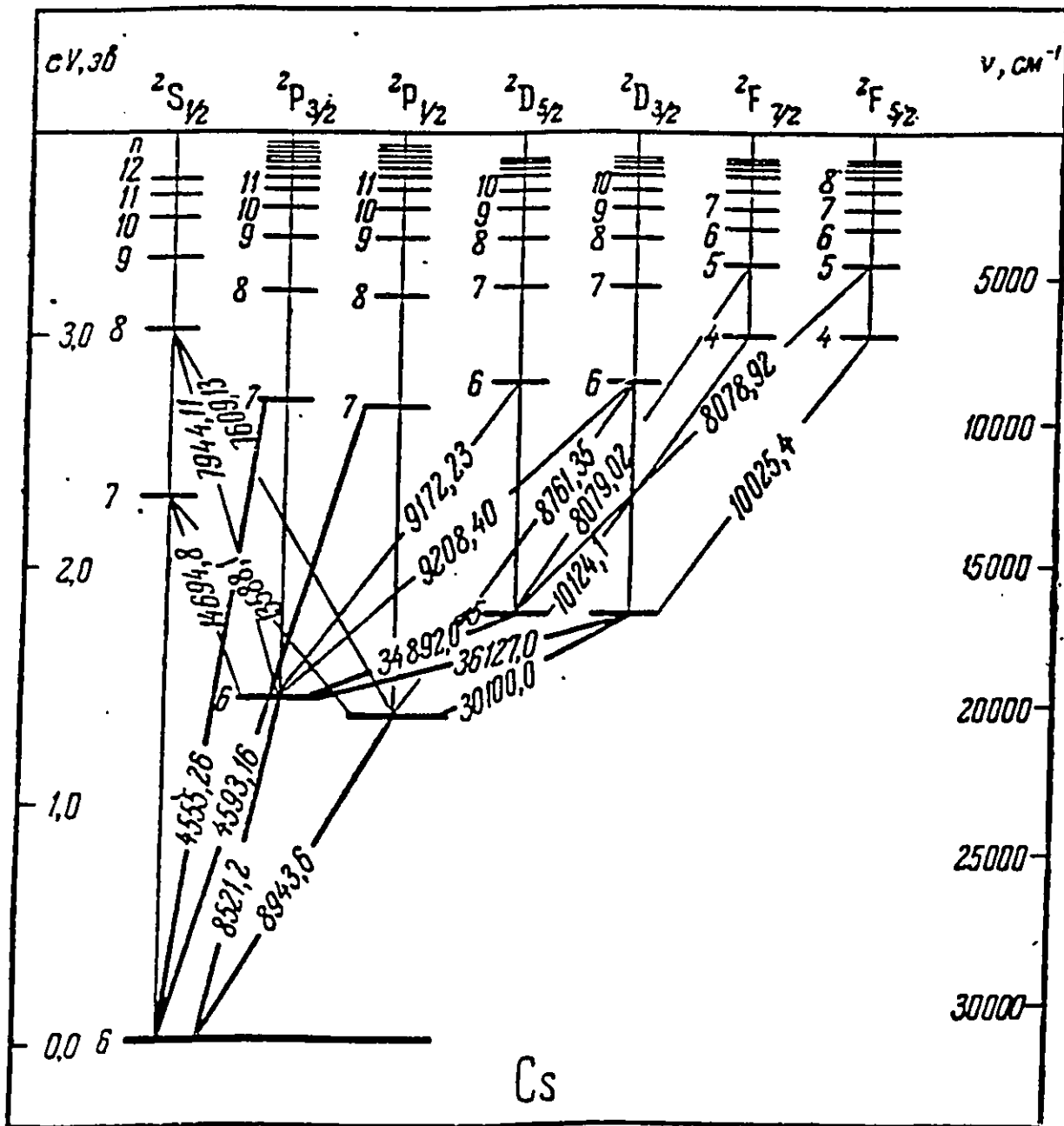
where τ_c is the duration of the collision.

We choose the interaction picture (IP) to discuss the problem, in which the Schroedinger equation is given by,

$$i\frac{d}{dt}\phi = \exp(iH_Bt)\,V(t)\,\exp(-iH_Bt)\,\phi = V^I(t)\,\phi \qquad (II.1.9)$$

where ϕ is any state in the IP. All quantities are stated in atomic units such that $\hbar = m_e = e = 1$

If the system is initially ($t=-\infty$) in state $|1\rangle$, then the time-evolved state $|t\rangle$ may be represented as follows by TDPT:

$$|t\rangle = [1 - i\int_{-\infty}^{t}dt_1\,V^I(t_1) - \int_{-\infty}^{t}dt_1\int_{-\infty}^{t_1}dt_2\,V^I(t_1)\,V^I(t_2) + \cdots]\,|1\rangle \qquad (II.1.10)$$

The probability of transition $|1\rangle \rightarrow |2\rangle$ is

$$P = |\langle 2|t\rangle|^2 \qquad (II.1.11)$$

The transition amplitude $\langle 2|t\rangle$ is evaluated by substituting eq.(II.1.10) into eq.(II.1.11) yielding, to second order,

$$\langle 2|t\rangle = \langle 2|1\rangle - i\int_{-\infty}^{t}dt_1\langle 2|V^I(t_1)|1\rangle - \int_{-\infty}^{t}dt_1\int_{-\infty}^{t_1}dt_2\langle 2|V^I(t_1)\,V^I(t_2)|1\rangle \qquad (II.1.12)$$

where the first term vanishes due to the orthogonality. The

6

second term, which represents the first-order perturbation, contains a matrix element

$$\langle 2|V^I(t_1)|1\rangle = \langle 2|e^{iH_Bt_1}V(t_1)e^{-iH_Bt_1}|1\rangle = e^{i(E_2-E_1)t_1}\langle 2|V(t_1)|1\rangle \qquad (II.1.13)$$

Using eqs. (II.1.3,4), we have

$$\langle 2|V(t)|1\rangle = -\alpha\langle 3/2,1/2|V(t)|1/2,-1/2\rangle$$

$$-\alpha\langle 1/2,1/2|V(t)|3/2,-1/2\rangle \qquad (II.1.14)$$

Eq.(II.1.14) incorporates the relation

$$\langle jm|V(t)|jm'\rangle = (-)^{(j-j'-m+m')}\langle j'-m'|V(t)|j-m\rangle \qquad (II.1.15)$$

representing "instantaneous" time-reversal symmetry, which leads to:

$$\langle 1/2,1/2|V(t)|1/2,-1/2\rangle = \langle 3/2,1/2|V(t)|3/2,-1/2\rangle = 0 \qquad (II.1.16)$$

The phase factor $\exp\{i(E_2-E_1)t_1\}$ in eq.(II.1.13) is slowly oscillating due to the fact that E_2-E_1 is small [see eq. (II.1.8)]. Thus compared to the second-order collisional contribution (see below), the contribution from $<2|V(t_1)|1>$ to the transition probability is not negligible even though the coupling constant α is small. This explains why a perturbative magnetic field has a substantial effect enhancing the m_J mixing cross section.

The first-order perturbation probability is expressed as

7

$$P^{(1)} = \left| \int_{-\infty}^{t} dt_1 e^{i(E_2 - E_1)t_1} \langle 2 | V(t_1) | 1 \rangle \right|^2 \qquad \text{(II.1.17)}$$

The integration (II.1.17) was actually done by converting the variable t to R which is the interatomic coordinate. In a real situation, R would be a very complicated function of time t which would make the integration difficult. I therefore used the straight-path approximation in which the coordinates and time are related more simply by

$$R = (b^2 + v^2 t^2)^{1/2} \qquad \text{(II.1.18)}$$

where b is the impact parameter and v is the relative speed between the collision partners, which is assumed constant during the collision.

V(t) is also converted to a function of space coordinates, becoming V(r,R), where r is the intra-atomic coordinate.

V(r,R) can be expanded in Legendre polynomials,

$$V(r, R) = \sum_L V_L(r, R) P_L(\hat{r} \cdot \hat{R}) \qquad \text{(II.1.19)}$$

By symmetry under spatial inversion and the triangular rule, only the L=2 terms contribute to the matrix element in eq. (II.1.19) and the matrix element of $V_2(r,R)$, $V_{211}(R)$, is found to have the approximate form

8

$$V_{211}(R) = C_n R^{-n} \qquad\qquad (II.1.20)$$

where C_n is a constant and n=5.46 was calculated for the Cs-He interaction (Baylis 1969).

Finally, the integration (II.1.17) must be averaged over all orientations of the collision frame with respect to the magnetic field, and the transition probability is found as a function of the impact parameter b

$$P(b) = \alpha^2 \frac{3}{5} \frac{n^2 - 3n + 3}{n^2} \left[\frac{2C_n}{5vb^{n-1}} \beta \left(1/2, \frac{n-1}{2} \right) \right]^2 \qquad\qquad (II.1.21)$$

where β is the beta function. For a given n, P(b) is simplified using eq.(II.1.5):

$$P(b) = \frac{\lambda B^2}{b^{n_1}} \qquad\qquad (II.1.22)$$

where $n_1 = 2(n-1)$ and λ is a constant

$$\lambda = \frac{2}{9} \left(\frac{\mu_0}{\Delta E} \right)^2 \frac{3}{5} \frac{n^2 - 3n + 3}{n^2} \left[\frac{2\beta \left(1/2, \frac{n-1}{2} \right)}{5v} \right]^2 C_n^2 \qquad\qquad (II.1.23)$$

which was further evaluated by substituting:

$\mu_0 = 2.127176 \times 10^{-6}$ a.u.

$\Delta E = 551$ cm$^{-1} = 2.511 \times 10^{-3}$ a.u.

$v = 5.93 \times 10^{-4}$ a.u.   [the average relative speed at room temperature (T=308K)]

9

$\beta(1/2,(n-1)/2)=1.255$ for n=5.46,

yielding

$$\lambda = 2.06 \times 10^{-1} C_n^2 \qquad\qquad\qquad (II.1.24)$$

Equation (II.1.21) gives the form of magnetic-field dependence of the transition probability as a function of b. With the knowledge of the transition probability, the Zeeman mixing cross section Q(1/2,-1/2→1/2,1/2) (denoted by Q) is obtained as

$$Q = \pi R_0^2 P(R_0) + 2\pi \int_{R_0} bdbP(b) = \pi R_0^2 \frac{n_1}{n_1 - 2} \frac{\lambda B^2}{R_0^{n_1}} \qquad (II.1.25)$$

where R_0 is the classical hard-core radius due to the strong repulsive interaction at small R. As an essential correction to the straight-path approximation, collision partners do not penetrate this hard-core region, and, accordingly, the integration of eq.(II.1.25) is performed from R_0 to infinity. The transition probability at smaller impact parameters is assumed equal to that at $b = R_0$. Eq.(II.1.25) also indicates that the cross section has a quadratic dependence on the field strength B (the 'field enhanced' part of the cross section).

There is still the second-order perturbation, the third term in eq.(II.1.12), which contributes a field-independent term to the cross section. The relevant matrix elements were

10

evaluated by inserting $|3/2,m>$ which are the substates of $6^2P_{3/2}$, with $m=\pm 3/2, \pm 1/2$. $|3/2,m>$ is not a complete set of substates, but it is a good approximation because all other states are distant and can be ignored in the process.

$$\langle 2|V^I(t_1) V^I(t_2)|1\rangle = \sum_m \langle 2|V^I(t_1)|3/2,m\rangle\langle 3/2,m|V^I(t_2)|1\rangle \qquad (II.1.26)$$

Bearing in mind the weak coupling in eqs. (II.1.3,4), the major part of each matrix element above is given by

$$\langle 2|V^I(t_1)|\frac{3}{2}m\rangle\langle\frac{3}{2}m|V^I(t_2)|1\rangle$$

$$\doteq \langle\frac{1}{2}\frac{1}{2}|V^I(t_1)|\frac{3}{2}m\rangle\langle\frac{3}{2}m|V^I(t_2)|\frac{1}{2}-\frac{1}{2}\rangle \qquad (II.1.27)$$

which is further evaluated by using eq.(II.1.9):

$$\langle\frac{1}{2},\frac{1}{2}|V^I(t_1)|\frac{3}{2},m\rangle\langle\frac{3}{2},m|V^I(t_2)|\frac{1}{2},-\frac{1}{2}\rangle$$

$$=e^{i\Delta E(t_1-t_2)}\langle\frac{1}{2},\frac{1}{2}|V(t_1)|\frac{3}{2},m\rangle\langle\frac{3}{2},m|V(t_2)|\frac{1}{2},-\frac{1}{2}\rangle \qquad (II.1.28)$$

This expression shows that collisions induce virtual transitions from the $6^2P_{1/2,-1/2}$ state to the substates of $6^2P_{3/2}$, and from there to the $6^2P_{1/2,1/2}$ state, without the participation

of the magnetic field. The transition probability as a function of impact parameter b can be calculated and gives the field-independent cross section Q_0. The probabilities of field-dependent and field-independent parts are summed rather than the transition amplitudes, because the cross term of these two amplitudes represents interference and is negligible after averaging over all orientations. Thus the total cross section is:

$$Q_T = Q_0 + Q = Q_0 + C_1 B^2 \qquad \text{(II.1.29)}$$

where the constant C_1 is given by

$$C_1 = \pi \frac{n_1}{n_1 - 2} \frac{\lambda}{R_0^{n_1 - 2}} \qquad \text{(II.1.30)}$$

The actual values of both Q_0 and C_1 can be calculated in the framework of the theory which requires accurate knowledge of the interaction potential and the hard-core radius. However, since C_1 and Q_0 are related to parameters like C_n [see eq.(II.1.16)] and R_0 which are only known with large uncertainties, I decided to derive C_1 and Q_0 from experimental data and in this way to obtain more information on the Cs + He interaction.

Here it would be appropriate to discuss the role played by the magnetic field. In the absence of the field, collisional interactions can not cause transitions from the

$^2P_{1/2,-1/2}$ state directly to $^2P_{1/2,1/2}$ state because of the "instantaneous" time-reversal symmetry [see eqs. (II.1.15) and (II.1.16)]; transitions can take place only by channels involving the $6^2P_{3/2}$ Zeeman substates as shown by eq. (II.1.27). The magnetic field breaks the symmetry by coupling the $^2P_{1/2}$ state to the $^2P_{3/2}$ state, and thus assists transitions between the $^2P_{1/2,-1/2}$ and $^2P_{1/2,1/2}$ states. One might think that this enhancement should be small for a perturbative field, because the coupling constant α is small. For example, $\alpha \approx 4 \times 10^{-4}$ when B=1T, and $|\alpha|^2$ will result in an even smaller value for the transition probability. But it is also necessary to consider the phase factors in eqs. (II.1.17) and (II.1.28), where the former equation oscillates much more slowly than the latter, due to relation (II.1.8). Thus the magnetic field-enhanced probability for a Zeeman transition in the $^2P_{1/2}$ state, relative to the field independent term, can be considerably larger than $|\alpha|^2$, and indeed a substantial enhancement of the cross section was observed experimentally.

Nevertheless, the magnetic-field-enhanced transition probability P(b) can not exceed unity, and the first-order Magnus approximation (Child 1974), as well as the evaluation of eq. (II.1.14), indicated that P(b) has a maximal value of 3/5. For strong collisions, P(b) oscillates between this maximum and zero with an average value of 3/10. This limit of probability affects the field-dependence of the cross section as illustrated in Fig.2. Fig.2(a) represents a plot of P(b)

against b; the upper curves correspond to stronger fields and, for the strongest field, there is a cutoff at P(b)=3/10. With the straight-path approximation, an impact parameter b corresponds to a cross section πb^2. Because the probability is a function of b, the total m_J mixing cross section Q is represented by the cylindrical volume indicated in Fig.2(b). This in accordance with eq.(II.1.25) where it is shown that the volume (or the mixing cross section) increases as B^2 when the maximum probability is below the limit 3/10. The volume will be truncated for probabilities above the 3/10 limit and consequently, the rate of enhancement of the cross section will decrease even as the field increases further. The cross section may now be expressed as:

$$Q = \pi b_0^2 P(b_0) + 2\pi \int_{b_0}^{\infty} b \, db \, P(b) = \pi b_0^2 \frac{n_1}{n_1 - 2} \frac{\lambda B^2}{b_0^{n_1}} \qquad \text{(II.1.31)}$$

where b_0 is defined to satisfy

$$P(b_0) = \frac{\lambda B^2}{b_0^{n_1}} = 0.3 \qquad \text{(II.1.32)}$$

The meaning of b_0 is interpreted in Fig.2 as the crossing point of the P(b) curve and the bound-line.

14

Figure 2. (a) Illustration of transition probability as a function of impact parameter b. $P(b)=0.3$ is the saturation line.

(b) Illustration of the corresponding Zeeman mixing cross section represented by the cylindrical volume.

P(b)

0.3

0.2

0.1

B_2

B_1

B_3

$B_1 < B_2 < B_3$

R_0 b_0

b

Fig.2 (a)

b

b
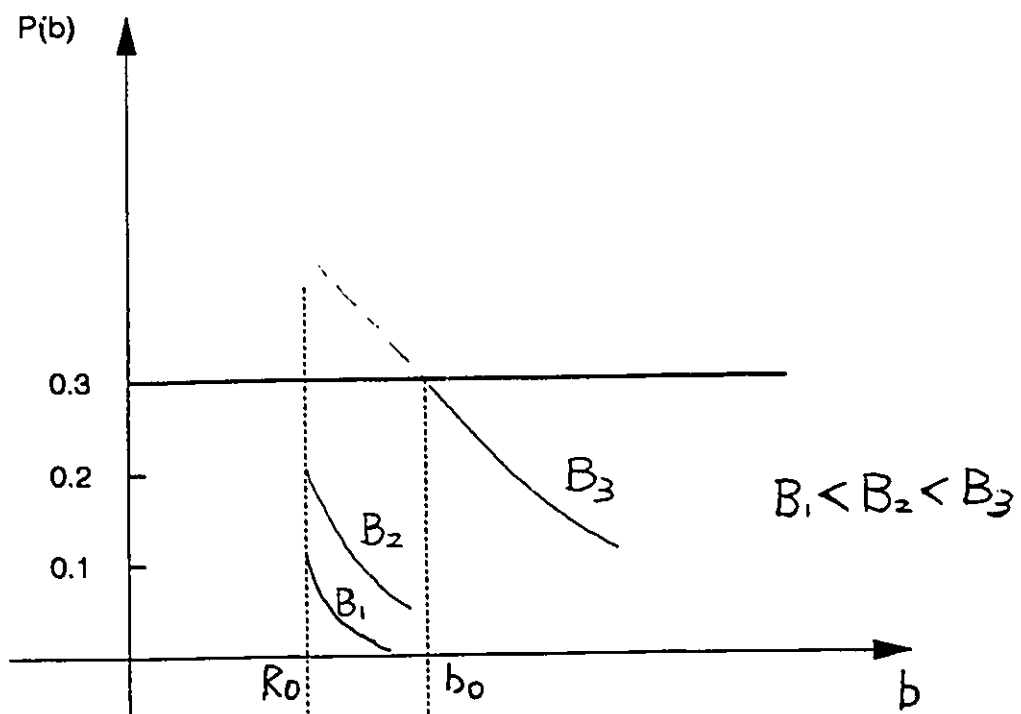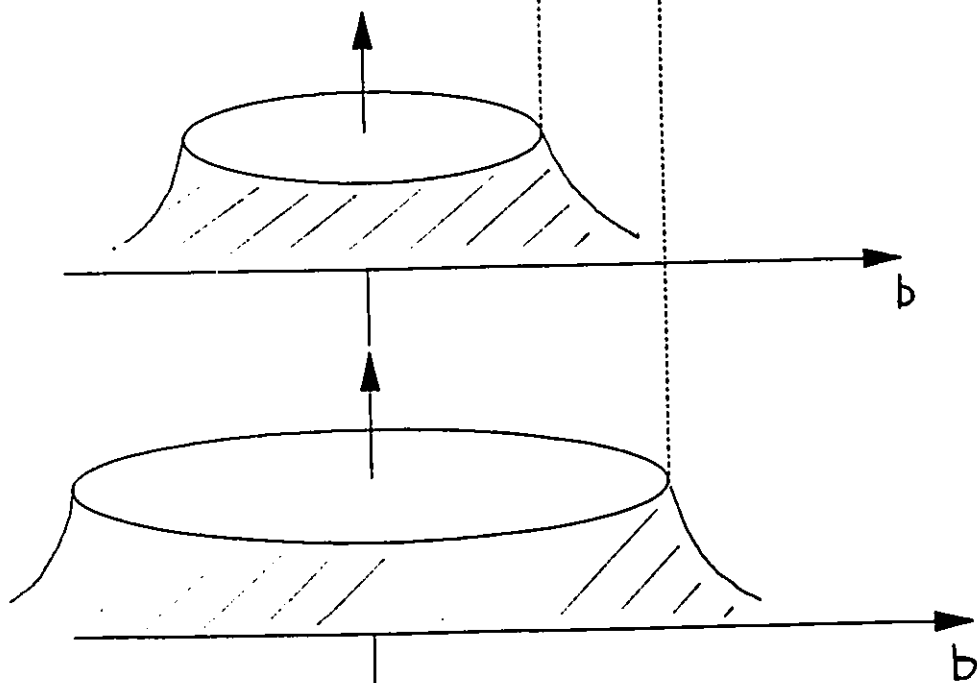
Fig.2 (b)

Substitution of eq.(II.1.32) into (II.1.31) gives the enhanced cross section at the 3/10 probability limit.

$$Q' = \pi \frac{n_1}{n_1 - 2} \frac{3}{10} \left(\frac{\lambda B^2}{0.3} \right)^{\frac{2}{n_1}}$$

(II.1.33)

Equation (II.1.33) indicates that Q' is proportional to $B^{2/8.92} = B^{0.45}$, for n=5.46, replacing the quadratic dependence on B which is predicted at lower fields. The total cross section is now given by

$$Q_T' = Q_0 + Q' = Q_0 + C_1' B^{\frac{2}{n_1}}$$

(II.1.34)

with the new constant C'_1 defined as:

$$C_1' = \pi \frac{n_1}{n_1 - 2} \frac{3}{10} \left(\frac{\lambda}{0.3} \right)^{\frac{2}{n_1}}$$

(II.1.35)

It may be seen from the above, that the theory predicts a change in the field-dependence of the cross section Q at a limiting magnetic-field strength ("turning point"), which can also be given in terms of R_0 and the fitting constant C_1. To do this, it is only necessary to know when the transition probability reaches the maximum value, represented in Fig.2 which shows when the probability curve begins to be cut off. The turning point of the field, B_{TURN} is given by:

16

$$\frac{\lambda B_{TURN}^2}{R_0^{n_1}} = 0.3 \qquad\qquad\qquad \text{(II.1.36)}$$

λ is explicitly related to the fitting constant C_1 by eq. (II.1.30):

$$\lambda = C_1 R_0^{n_1-2} \frac{n_1-2}{\pi n_1} \qquad\qquad\qquad \text{(II.1.37)}$$

Using eqs. (II.1.36,37), B_{TURN} can be expressed in terms of C_1 and the hard-core radius R_0:

$$B_{TURN} = (\frac{3\pi}{10} \frac{n_1}{n_1-2} \frac{R_0^2}{C_1})^{1/2} \qquad\qquad\qquad \text{(II.1.38)}$$

As the result of this calculation, it is possible to predict the general form of the field dependence of the cross section Q.

$Q_T = Q_0 + C_1 B^2 \qquad\qquad (B < B_{TURN})$

(II.1.39)

$Q_T = Q_0 + C'_1 B^{0.45} \qquad\qquad (B \geq B_{TURN})$

(II.1.40)

Equations (II.1.39,40) indicate that the enhanced cross section will change its dependence on the field B at a particular field strength B_{TURN}. At lower fields, the quadratic dependence of the mixing cross section has already been

17

confirmed experimentally by Guiry and Krause (1975). A fit of eq.(II.1.39) resulted in the following predicted magnetic-field dependence of the Zeeman mixing cross section over the complete range of magnetic field **B** from zero to 7T.

$$Q_T = 10.7 + 14.6B^2 \text{ a.u.}$$
$$= 3 + 4.1B^2 \quad Å^2 \qquad (B < 0.76T)$$
$$= 10.7 + 9.67B^{0.45} \text{ a.u.}$$
$$= 3 + 2.71B^{0.45} \quad Å^2 \qquad (B \geq 0.76T)$$

A detailed comparison of these prediction with the experimental results will be made in Chapter IV.

II.2   Derivation of the $6^2P_{1/2}$ Zeeman Mixing Cross
        Section from intensities of the Zeeman
        fluorescence components

When Cs vapour containing atoms excited to the $6^2P_{1/2}$
state is placed in a magnetic field, the $6^2P_{1/2}$ and $6^2S_{1/2}$ are
split into magnetic (Zeeman) sublevels, as shown in Fig.3. The
sublevels correspond to substates denoted by magnetic quantum
numbers m_j. Although each substate can be further split into
hyperfine structure components due to nuclear spin, it will be
shown that nuclear spin coupling does not contribute much to
the mixing of the Zeeman substates. Figure 3 shows the σ
transitions for which $\Delta m_j = \pm 1$; the π transitions ($\Delta m_j = 0$) are not
shown.

Collisions between the excited Cs atoms in their Zeeman
substates and He atoms cause Zeeman mixing, described by the
following equation:

$$\text{Cs}(6^2P_{1/2,-1/2}) + \text{He}(^1S_0) + \Delta E_{1/2,-1/2} = \text{Cs}(6^2P_{1/2,1/2}) + \text{He}(^1S_0) \qquad (II.2.1)$$

where $\text{Cs}(6^2P_{1/2,-1/2})$ and $\text{Cs}(6^2P_{1/2,1/2})$ are Cs atoms in their two
Zeeman substates of the $6^2P_{1/2}$ resonance fine structure state,
and $\text{He}(^1S_0)$ is a ground-state He atom. $\Delta E_{1/2,-1/2}$ is the energy
difference between the two substates $m_j = 1/2$ and $m_j = -1/2$, the
magnitude of which is dependent on the magnetic field
strength. The transitions between $6^2P_{1/2}$ and $6^2P_{3/2}$ states are
neglected due to the large energy gap of 551 cm^{-1} (the fine-

Figure 3. Energy level diagram of the Cs $6^2S_{1/2}$ and $6^2P_{1/2}$ Zeeman substates, showing the σ transitions. The $6^2P_{1/2,-1/2}$ substate is optically excited. The π transitions are not shown. The separation of the energy levels are not shown to scale.

m_J

$6\,^2P_{1/2}$ ½
  -½

σ^- σ^+

$6\,^2S_{1/2}$ ½
  -½

20
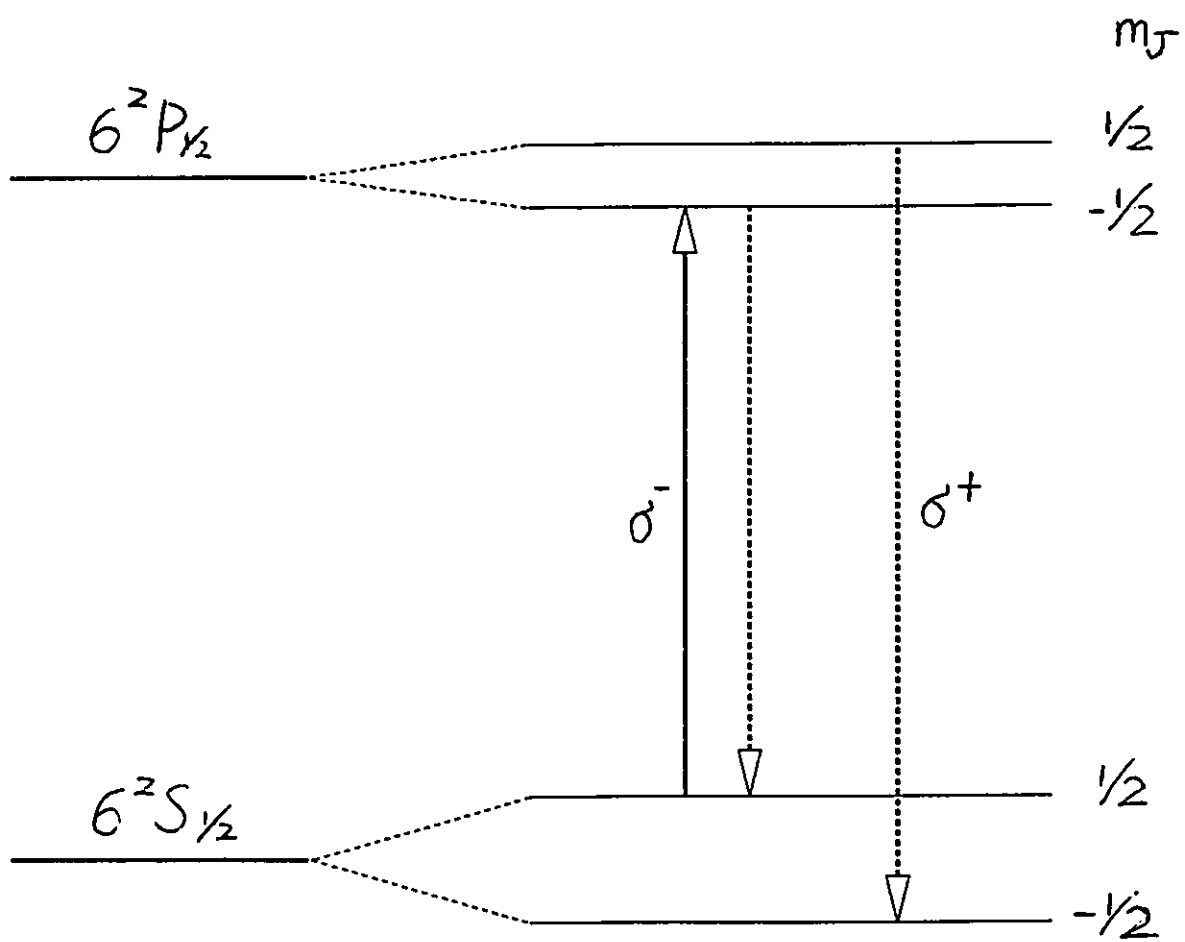
When the $6^2P_{1/2,-1/2}$ state is populated by laser excitation, the time evolution of the two Zeeman substates may be described by the rate equations:

$$\frac{dn_-}{dt} = S_-(t) - \frac{n_-}{\tau} - Z_{-1/2,1/2}n_- + Z_{1/2,-1/2}n_+ \qquad \text{(II.2.2)}$$

$$\frac{dn_+}{dt} = -\frac{n_+}{\tau} + Z_{-1/2,1/2}n_- - Z_{1/2,-1/2}n_+ \qquad \text{(II.2.3)}$$

$S_-(t)$ is the excitation rate of the $m_j = -1/2$ state; n_-, n_+ are the densities of the atoms in the $m_j = 1/2$ and $m_j = -1/2$ substates, respectively; $Z_{-1/2,1/2}$ and $Z_{1/2,-1/2}$ are the collision numbers (defined as number of collisions per excited Zeeman atom and per second) corresponding to the transitions $m_j = -1/2 \rightarrow m_j = 1/2$ and $m_j = 1/2 \rightarrow m_j = -1/2$ within the $^2P_{1/2}$ state, respectively. $\tau = 34$ ns is the average lifetime of the $^2P_{1/2}$ state (Link 1966). The general solutions of the eqs.(II.2.2,3) are integrated to give

$$n_\pm = \frac{1}{2} \int_0^\infty e^{-\frac{T}{\tau}} (1 \mp e^{-2ZT}) S_-(t-T) \qquad \text{(II.2.4)}$$

where it is assumed that $n_\pm(-\infty) = 0$.

The integrated populations are defined as

$$N_\pm = \int_{t_0}^\infty dt\, n_\pm(t) \qquad \text{(II.2.5)}$$

21

The integration is carried out from t_0 instead of $-\infty$ because a delay time was used in the experiment to avoid scattered light. [see chapter III (e)]. The explicit expression for the integrated population is then found to be:

$$N_\pm = \frac{1}{2} \int_{t_0}^{\infty} dt \int_0^{\infty} dT\, e^{-\frac{T}{\tau}} (1 \mp e^{-2zT})\, S_-(t-T)$$ (II.2.6)

The $m_j = -1/2$ state was excited with a pulsed dye laser and, considering also the distribution of excitation pulses, the excitation rate may be best expressed as

$$S_-(t) = \int_{-\infty}^{\infty} dt_1 S_1(t_1)\, \delta(t-t_1)$$ (II.2.7)

where a gaussian distribution is assumed, expressed by

(II.2.8)

$$S_1(t_1) = S_1(0)\, e^{-\frac{t_1^2}{\Delta^2}}$$

the half-width Δ of the exciting laser pulse was measured to be 3.5 ns.

The measured fluorescence intensities, I_- and I_+ for σ^- and σ^+ transitions, respectively, are proportional to the products of the integrated populations and Einstein A coefficients,

$$I_- = AN_-;\ I_+ = AN_+$$ (II.2.9)

22

The same A coefficient is used for both transitions as the A coefficients for the σ^- and σ^+ transitions are very nearly equal to one another.

The measured intensity ratio η is defined as:

$$\eta = \frac{I_+}{I_-} = \frac{N_+}{N_-} \tag{II.2.10}$$

Equations (II.2.6,10) yield,

$$\eta = \frac{1 + 2Z\tau - \exp(-2Zt')}{1 + 2Z\tau + \exp(-2Zt')} \tag{II.2.11}$$

where $t' = t_0 - Z\Delta^2/2$

and, from detailed balancing,

$$Z_{-1/2,1/2} = Z_{1/2,-1/2} = Z \tag{II.2.12}$$

The collision number Z is generally related to the transfer cross section Q which is defined analogously to the gas-kinetic cross section :

$$Z_{ab} = NQ(a,b)v_r \tag{II.2.13}$$

$Q(a,b)$ is the cross section for transition from state a to b, N is the density of the He gas and v_r is the average relative speed of the colliding partners whose reduced mass is μ

$$v_r = (8kT/\pi\mu)^{1/2} \tag{II.2.14}$$

k is the Boltzmann constant and T is the absolute temperature of the vapour-gas mixture. According to the principle of detailed balancing, the cross sections $Q(1/2,-1/2 \rightarrow 1/2,1/2)$ and

23

$Q(1/2,1/2\rightarrow1/2,-1/2)$ should be in the ratio

$$\frac{Q(1/2,1/2\rightarrow1/2,-1/2)}{Q(1/2,-1/2\rightarrow1/2,1/2)}=\exp(-\frac{\Delta E}{kT})$$ (II.2.15)

Since the Zeeman splitting $6^2P_{1/2,\pm1/2}$ is much smaller than kT at room temperature, eq.(II.2.12) results.

The exponential in eq.(II.2.11) is expanded to yield an approximate expression for η:

$$\eta\approx Z(\tau+t')-Z^2\tau^2+Z^3\tau^3(1-\frac{t'}{\tau}-\frac{t'^2}{\tau^2}-\frac{t'^3}{3\tau^3})-\cdots$$ (II.2.16)

Keeping the approximation terms up to the second-order of $(Z\tau)^2$, gives

$$\eta\doteq Z(\tau+t_0)-Z^2(\tau^2+\Delta^2/2)$$ (II.2.17)

Careful consideration was given to the spread of the delay time (jitter), since some of the detected pulses were delayed more than others as they passed through the detection electronics (the photomultiplier and the gated pulse sampler). The result was a distribution of detected pulses with different delays t_0 relative to the excitation-pulse maximum before the particular group of pulses began to be counted. The expressions for $N_\pm$ can be averaged over this distribution and the final corrected expression for η is:

$$\eta \doteq Z(\tau + t_0 - \frac{\delta^2}{2\tau}) - Z^2 [\tau^2 + \frac{1}{2}(\Delta^2 + \delta^2)] \qquad\qquad (II.2.18)$$

where δ is the jitter (ns)

Equation (II.2.18) provides the connection between the measured relative intensities of the fluorescence components and the cross section $Q(1/2, -1/2 \to 1/2, 1/2)$, provided the parameters are known. Equation (II.2.18) will be fitted to the experimental data to obtain the cross section Q, and the validity of the approximation is corroborated by the experimental results.

III   THE APPARATUS AND EXPERIMENTAL PROCEDURES

III.1   Description of the apparatus

The arrangement of the apparatus is shown schematically in Fig.4. Cs vapour, mixed with helium and contained in a fluorescence cell located at the centre of a superconducting solenoid, was irradiated with pulses from a N_2 laser-pumped dye laser which excited the Cs atoms to one of the $6^2P_{1/2}$ Zeeman substates. The selection of the exciting wavelength was achieved with the aid of a thermionic diode. The resulting partly circularly polarized fluorescence, monitored at right-angles to the direction of excitation and parallel to the magnetic field, was condensed by a lens and was made incident perpendicularly on the mirrors of a piezoelectrically scanned Fabry-Perot interferometer. The interferometer output was focused onto the photocathode of a cooled photomultiplier. The output of the latter was amplified , gated, and accumulated in a multichannel scaler .

(a) The N_2 Laser and Dye Laser System

The N_2 laser and dye laser were both manufactured in house. The N_2 laser had an output energy of ?mJ per pulse and was operated at a repetition rate of about 12 Hz. The dye laser consisted of an oscillator and an amplifier.

Figure 4. A Schematic arrangement of the apparatus for the measurement of the Zeeman mixing cross sections. N_2L, nitrogen laser; DL, dye laser; PD, photodiode; D, delay line; A, vacuum and gas filling system; FP, Fabry-Perot scanning interferometer; PM, photomultiplier tubes; S1, S2, shutters; AMP, amplifier-discriminator; GATE, gated pulse-inverter amplifier; LT, channel advance and laser trigger controller; SC, shutter controller; B, magnetic field.

B

CELL

PD

DL

N₂ L

D

FP

HeNe L

S1

SC

DAS 10

RAMP

T

PM2

S2

PM1

AMP

GATE

MCS

LT

27
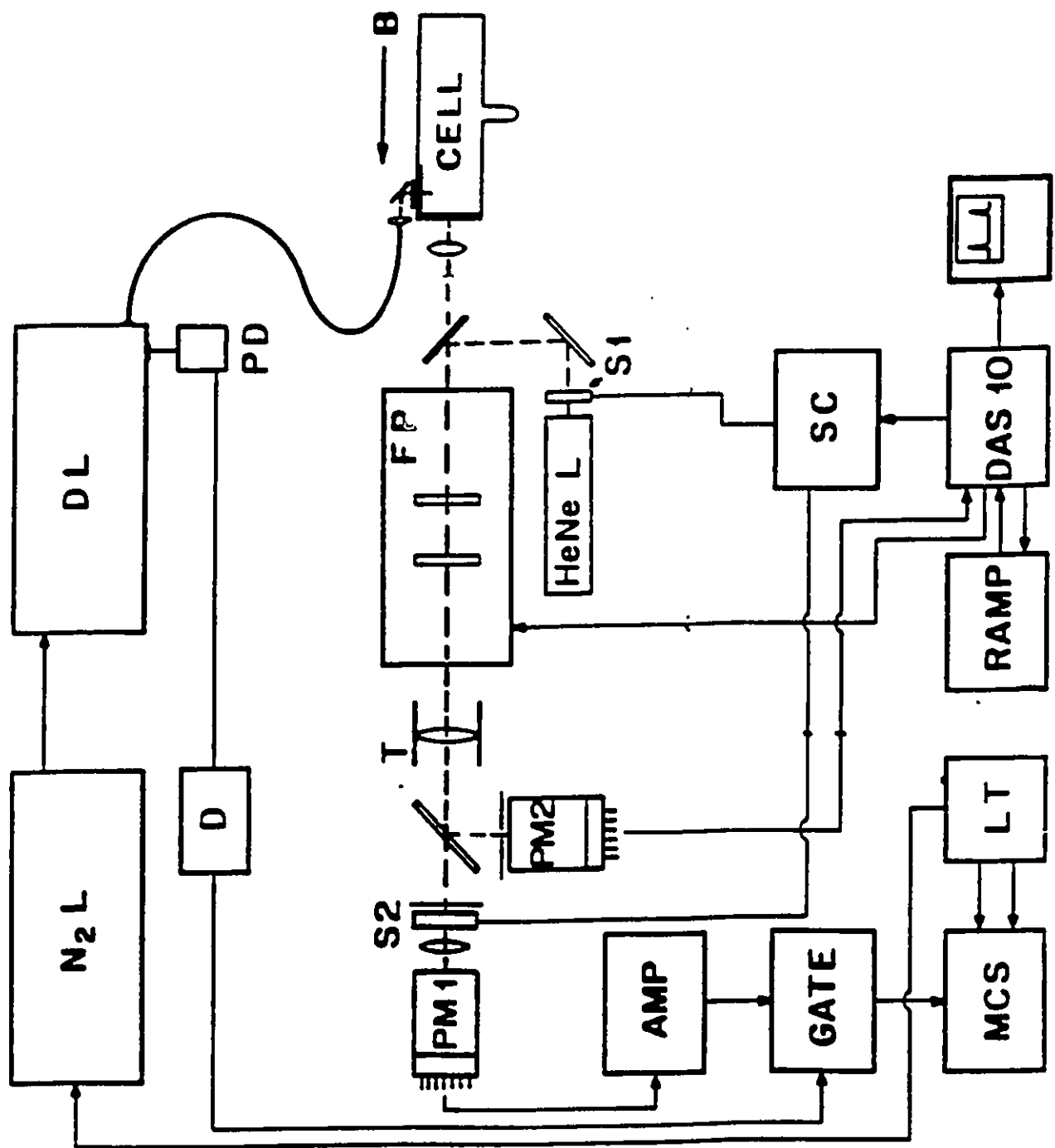
The oscillator incorporated a holographic 1800 l/mm grating , an achromatic beam expander and a reflection mirror. The grating was mounted on a sine-drive tuning arm driven by a stepping motor which produced a minimum step corresponding to a wavelength interval of 0.125 $\text{\AA}$.

The beam expander, which contained two sets of double prisms in order to achieve both zero beam-dispersion and zero-beam deviation, was developed earlier (Niefer and Atkinson 1988). The output beam of the prism expander was parallel to the input beam, which enabled the stepping motor to produce a linear wavelength-scan of the dye-laser beam. A lens which was placed in line between the oscillator and the amplifier of the dye laser ,focused the laser beam from the oscillator into the dye cell of the amplifier. This improved the performance of the amplifier of the dye laser and produced a higher output energy. IR-125 ($C_{43}H_{47}N_2O_6S_2Na$) dye was used, dissolved in DMSO (Dimethyl sulphoxide) at a concentration of $1.67\times10^{-3}M$. Its working range was from 879 to 943 nm and it could be used for up to 10 hours without dramatic decline in the output power.

The output beam from the dye laser was coupled through a lens into a UV-NIR transmissive multimode optical fibre supplied by Newport Industries. The laser beam was conveyed through the fibre to a termination consisting of a lens and mirror which directed it into the fluorescence cell, at right angles to the direction of observation.

(b) The Fluorescence Cell and the Oven

The quartz cell had a square cross section and dimensions 2.5×2.5×4.0 cm, and was fitted with a 1 cm-long sidearm which protruded downwards and contained a small quantity of Cs metal. The cell was connected to the vacuum system through a capillary tube and a greaseless teflon stopcock. The cell and the sidearm were mounted in an oven located in a brass tube extending from the mounting of the vacuum system into the bore of the superconducting solenoid. The oven surrounding the cell was made of thick copper plates containing channels through which silicone oil was circulated. The sidearm oven, mounted beneath the main oven and insulated from it , consisted of windings of narrow-bore copper tubing in thermal contact with the sidearm of the cell , through which silicone oil was circulated. The heated silicone oil was circulated by Neslab thermostats, controlling the temperatures of the two ovens.The temperatures of the cell and the sidearms were monitored with 5 thermocouples located at various points on the cell and referenced to the triple point of water

(c) The Vacuum and Gas-filling System

The vacuum system consisted of an Edwards 2" diffu ion pump, a liquid Nitrogen trap and an Edwards EM2 forepump .The ultimate vacuum attainable by the system was of the order of

29

7×10^{-8} torr which was measured by an RG1000 Veeco ionization gauge. The gas-filling system consisted of pyrex bottles, separated from the vacuum system by individual teflon stopcocks, as well as a main stopcock and a microleak valve which was used to admit controlled quantities of helium (a Research Grade product from Union Carbride Corporation, Linde Division) to the cell. Gas pressures were measured with an MKS Baratron capacitance gauge ,which had been found previously to be working linearly up to 10 torr. A series 275 convectron vacuum gauge manufactured by Granville-Phillips was also used for gas pressures above 1 torr.

(d) The Superconducting Magnet.

The superconducting magnet , an Oxford Instruments (Mod. S7/123/1) superconducting solenoid, was capable of generating magnetic fields up to 7 T with a specified homogeneity of 1% within 11mm of the centre of the coil along its axis. The solenoid had a room-temperature access bore in which was placed the fluorescence cell and oven assembly. The magnet assembly consisted of a 100 L liquid nitrogen reservoir connected to a lower liquid helium reservoir surrounded by a vacuum containment vessel and several internal heat shields. The liquid helium boil-off rate was found to be approximately 4 L/day and the liquid helium level was monitored by a level-meter on the panel of the power supply. The magnet was mounted

on a wheeled platform which moved on rails fixed to the concrete floor. This arrangement allowed easy access to the oven and cell assembly for the occasional alignment of the optical components positioned at the centre of the solenoid, and also permitted the vacuum system to remain fixed.

(e) The Interferometer and Data Acquisition System

The output fluorescence signal was sent into the detection system which consisted of a piezoelectrically scanned Fabry-Perot interferometer and a gated photomultiplier.

A Burleigh Mod.110 scanning interferometer was used to resolve the Zeeman fluorescence. The instrument contained two broadband mirrors (λ/200 flat) having an average reflectivity of 94±2% ; one of the mirrors was attached to the piezoelectric transducers. The instrument, having a finesse of about 30 and a free spectral range of about 10 cm^{-1}, was sufficient to resolve the two peaks constituting the Zeeman fluorescence spectrum. One peak was due to the direct fluorescence and the other to the sensitized fluorescence induced by the collisions with the He atoms. A Burleigh programmable ramp generator (RC-43) and Fabry-Perot stabilization system (DAS-10) were used to scan and stabilize

the interferometer . An analogue high voltage ramp from the ramp generator, applied to the piezoelectric transducers attached to one mirror, produced repetitive scans extending from one to two interference orders. The Burleigh DAS-10 unit was used to stabilize the interferometer. This instrument actively corrected the interferometer alignment by locking it to an interference pattern produced by a He-Ne laser in a particular time segment of the scan . Within this time segment it adjusted automatically the spacing and alignment of the interferometer cavity to maintain the He-Ne peak at its maximum peak amplitude. This automatic feed-back arrangement resulted in a stable average fringe pattern with a high average finesse. The output of the photomultiplier was sent to a gated pulse sampler which was manufactured in-house. The pulse sampler was triggered by a delayed signal from a fast photodiode which was activated by the firing of the N_2 laser. The delay, which was set for the minimal time sufficient to avoid the direct scattered light from the dye laser, was measured to be about 35 ns from the pulse centre. The pulse sampler was connected to the multichannel scaler which recorded the signal in 512 channels . Several channels of the multichannel scaler were not used for the registration of fluorescence signals as they were located in the time segment corresponding to the operation of the DAS-10 unit.

Two shutters were used as part of the optical system; one was placed in front of the He-Ne laser, the other was located

in front of the photomultiplier . A shutter controller opened and closed the shutters in sequence. The first, when open, allowed the He-Ne beam to pass through the interferometer and the transmitted signal was used by the DAS-10 unit to stabilize the interferometer. The second shutter remained open for the two-second scan of the interferometer, enabling the photomultiplier PM1 to detect the fluorescence.

The whole detector system was synchronized . A fast photodiode detecting the Nitrogen laser pulse triggered the pulse sampler (after a delay time) .A separate trigger pulse was produced by the ramp generator at the beginning of each scan and was sent to the shutter controller and the multichannel scaler which registered the output pulses from the photomultiplier.

A microcomputer (PC AT clone) was connected to the multichannel scaler.After sufficient fluorescence signal had been accumulated in the multichannel scaler, the data in it were transferred to the microcomputer for further analysis and plotting.

(f) The Cs Thermionic Diode.

The thermionic diode (TD) was used to accurately set the dye-laser wavelength for the excitation of the Cs $6^2P_{1/2}$ state. The thermionic diode employed a cylindrical anode and cathode, and was enclosed in a glass tube 14 cm long and 2.5 cm in

diameter, fitted with a sidearm containing a small quantity of Cs metal. The diode also contained 0.2 torr argon to sustain its operation. It was housed in an electrically heated oven at a temperature of 160 °C. The sidearm temperature was held at a few degrees lower to avoid condensation of cesium on the input window. The voltage applied to the electrodes was about 50 V, just above the voltage required to maintain a glow discharge;, a somewhat higher voltage was applied in order to increase the signal when aligning the dye laser. An oscilloscope , triggered by a fast photodiode, was used to monitor the potential across a 40.4 kΩ resistor connected in series with the TD electrodes. When the laser was tuned to an atomic transition, a voltage spike would occur and would appear on the oscilloscope screen , thus fixing the wavelength for the excitation of the $6^2 P_{1/2}$ state in the absence of the magnetic field, which served as a reference for the Zeeman splitting. The TD facilitated the simple and rapid dye-laser tuning to the transitions in Cs, and was used for the wavelength calibration of the dye-laser (over a limited wavelength range).

III.2   Experimental Procedure

To produce a satisfactory intensity of the exciting radiation in the cell, considerable effort was devoted to align the dye-laser and couple the dye-laser output through a

lens into the optical fibre which conveyed the laser radiation to the termination at the entrance window of the fluorescence cell. The superconducting magnet and the optical system were aligned and adjusted so that the axis of the detection system was collinear with the axis of the superconducting solenoid. The stabilization of the interferometer was verified using the DAS-10 unit referenced to the He-Ne laser. The fluorescence cell and sidearm were baked under vacuum for some days until a vacuum of about 7×10^{-8} torr was reached. The cesium metal was vacuum-distilled into the sidearm, and both the cell and sidearm ovens were turned on and allowed to stabilize over a period of 24 hours.

Before filling with liquid helium, the magnet was precooled with liquid nitrogen for at least 12 hours. After filling with liquid helium, 12 additional hours were allowed to elapse before turning on the magnetic field, to ensure that the whole system reached full thermal equilibrium.

For each experimental run performed at a different magnetic field strength, the free spectral range of the interferometer was checked to ensure that the peaks of the direct fluorescence and of the fluorescence emitted from the collisionally populated $6^2P_{1/2}$ Zeeman substates were properly resolved. A relatively high pressure of the helium (about 5 torr) was used for this purpose in order to obtain a satisfactory signal in a short time.

At each magnetic field strength and the corresponding

Zeeman splitting, the experiment was performed with several helium pressures ranging from 0 to 5 torr, at intervals of about 0.5 torr. About 1000 scans of the interferometer were made in experimental runs at higher He pressures, and those at lower pressures required about 2000 scans. After sufficient data were recorded to obtain a satisfactory signal to noise ratio, they were transferred to the computer for diagram-plotting and further analysis. In order to select the correct wavelength-setting of the dye laser to excite the $^2P_{1/2,-1/2}$ Zeeman state at each magnetic field strength, the Zeeman splitting for $6^2P_{1/2}$ and $6^2S_{1/2}$ states and the wavelengths of σ^- transitions were calculated and are listed in Table 1.

Table 1. Zeeman splittings $\Delta\nu$ of the Cs $6^2S_{1/2}$ ground state and the $6^2P_{1/2}$ resonance f.s. state, and wavelengths λ of σ^--transitions at various magnetic-field strengths

B(T)	Zeeman Splittings (cm^{-1})		$\lambda(\sigma^{--\text{transition}})$
	$6^2S_{1/2}$	$6^2P_{1/2}$	(Å)
0	0	0	8943.599
0.5	0.466898	0.155633	8943.849
1.0	0.933795	0.311267	8944.097
1.5	1.400693	0.466900	8944.345
2.0	1.867591	0.622534	8944.596
2.5	2.334488	0.778167	8944.844
3.0	2.801386	0.933800	8945.094
3.5	3.268284	1.089433	8945.342
4.0	3.735181	1.245067	8945.592
4.5	4.202079	1.400701	8945.840
5.0	4.668977	1.556334	8946.090
5.5	5.135875	1.711968	8946.340
6.0	5.602772	1.867601	8946.588
6.5	6.069670	2.023234	8946.838
7.0	6.536567	2.178868	8947.087

IV   RESULTS AND DISCUSSION

The recorded fluorescence signals for various magnetic field strengths (in the range 1.5 - 7 T) and He pressures are shown in Fig.5(a)-(i). Effects of increasing He pressures at each (constant) magnetic field strength are shown in each figure, providing a clear demonstration of how the ratios η between sensitized fluorescence and direct fluorescence intensities depend on He pressure. The interferograms were smoothed by averaging the signals from 20 consecutive channels. The intensity ratios were measured and corrected by subtracting the background noise values. The intensity ratios are connected to the cross section through relation (II.2.18), and the cross section Q is obtained by least-squares fitting of eq.(II.2.18) which is more explicitly written as:

$$\eta \doteq QNv_r\tau\,(1+\frac{t_0}{\tau}-\frac{\delta^2}{2\tau}) - (QNv_r\tau)^2(1+\frac{\Delta^2+\delta^2}{2\tau^2}) \qquad (IV.1)$$
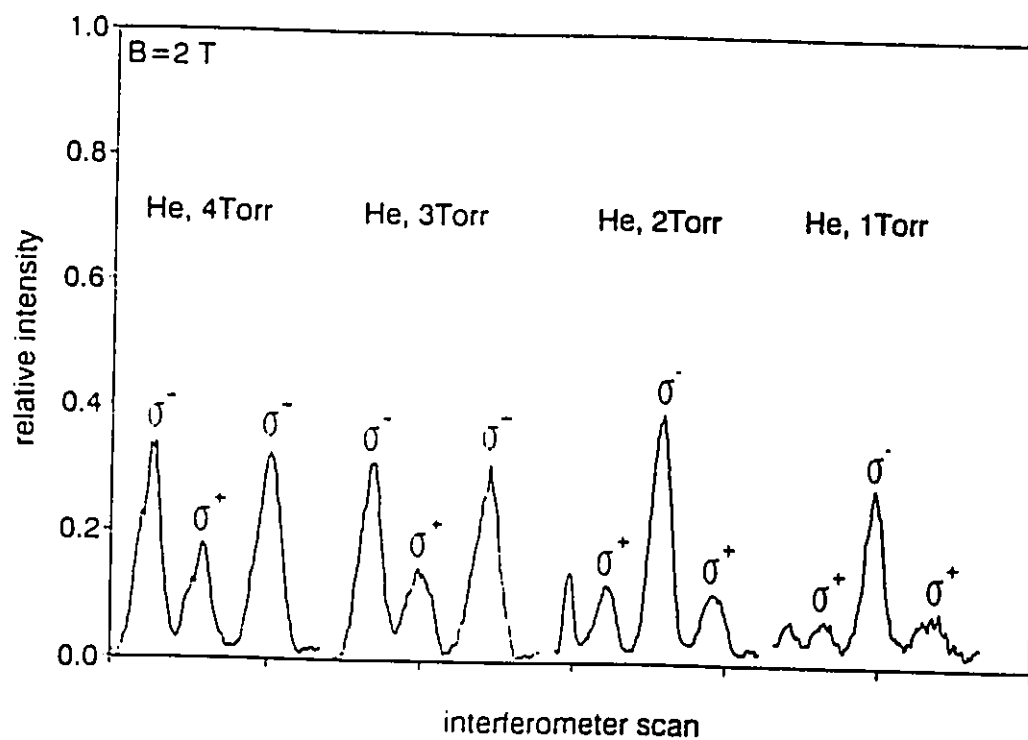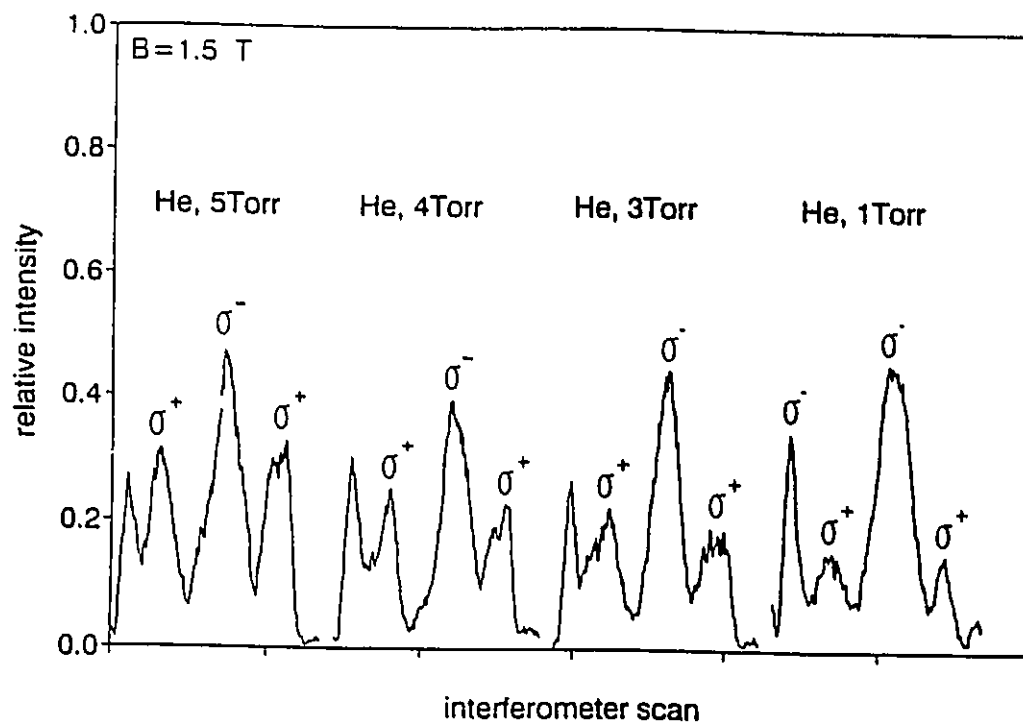
where $Nv_r\tau$ is a function of pressure P and temperature T of helium. If the gas is assumed to be ideal,

$$Nv_r\tau = 2.422\times10^{19}\times\frac{P}{\sqrt{T}} \qquad (IV.2)$$

with P measured in torr and T in Kelvin.

Plots of η against $Nv_r\tau$ are shown in Fig.6(a)-(i) for the

38

Figure 5. Interferograms of the Zeeman fluorescence spectrum emitted from the Cs $6^2P_{1/2}$ state excited with σ^- light, in a Cs + He mixture, at various magnetic field strengths. Peaks labelled σ^- represent resonance fluorescence and peaks labelled σ^+ represent sensitized fluorescence due to collisional transitions.

Fig.6(a) B=1.5T

Fig.6(b) B=2T

44

Fig.6(c) B=2.5T

Fig.6(d) B=3T

Fig.6(e) B=3.5T

Fig.6(f) B=4T

Fig.6(g) B=5T

Fig.6(h) B=6T

47

Fig.6(i) B=7T

INTENSITY RATIO

He PRESSURE(Torr)

48
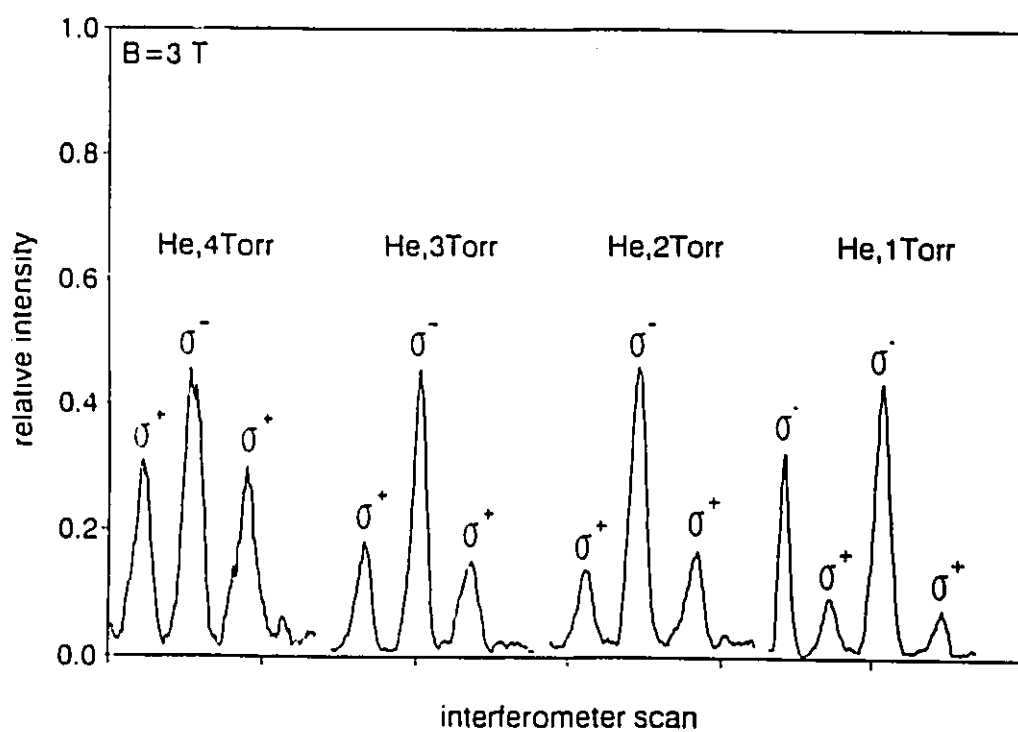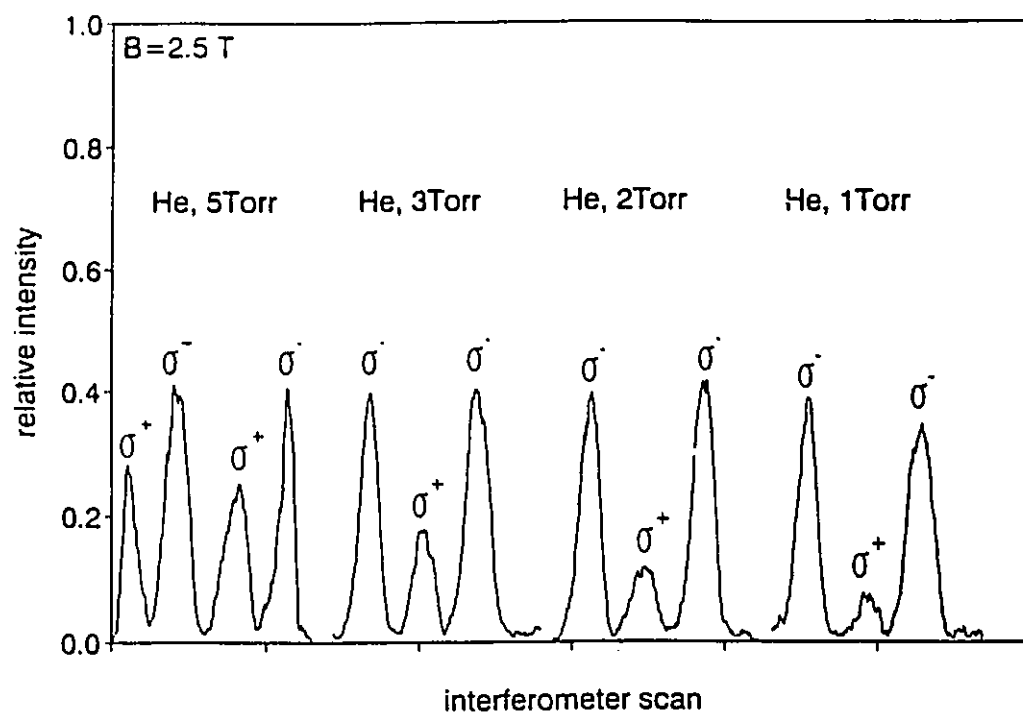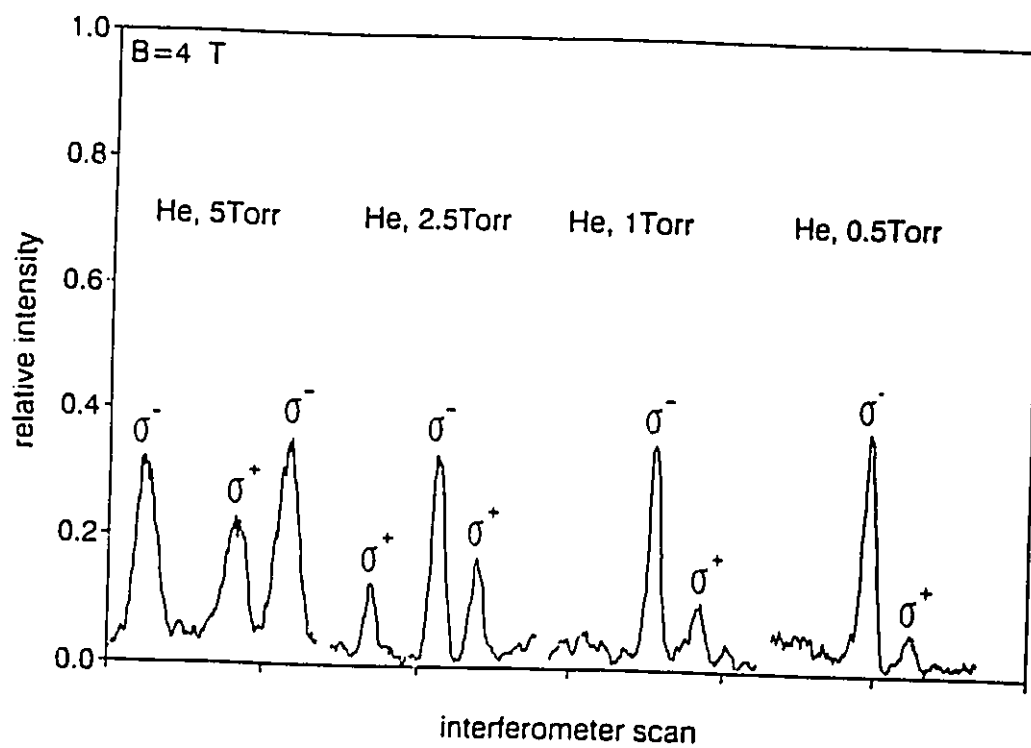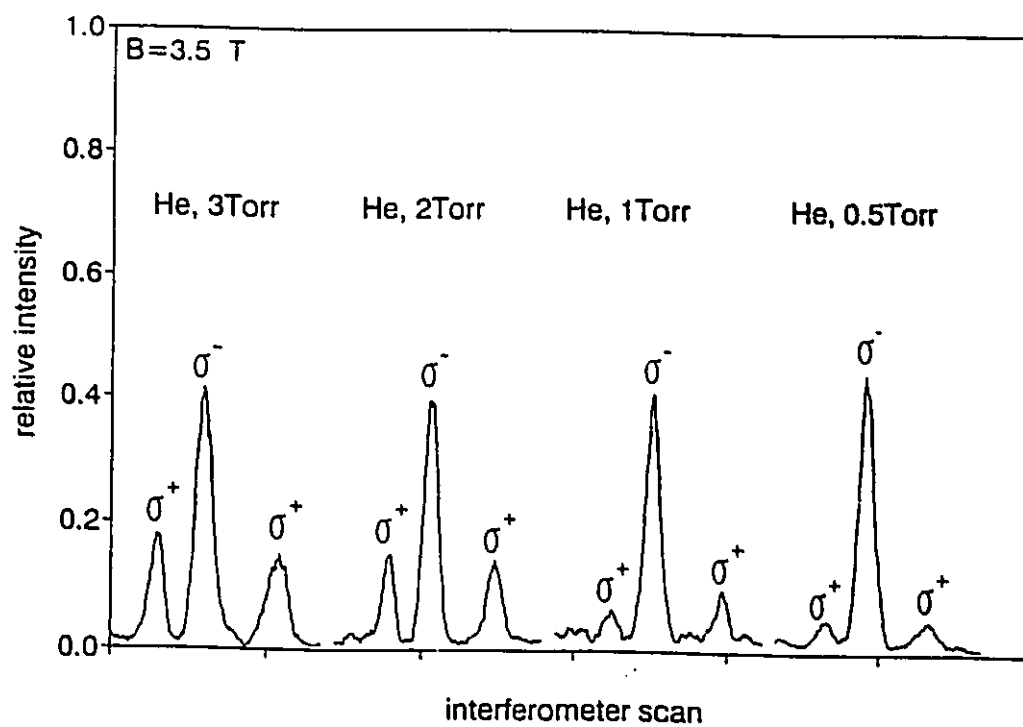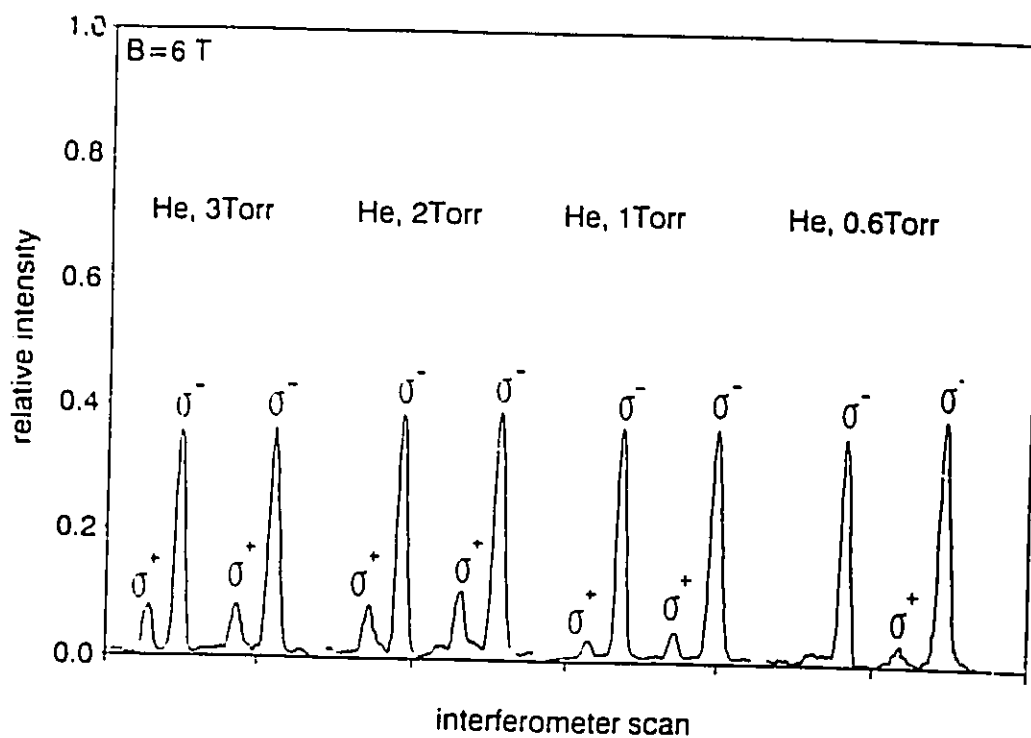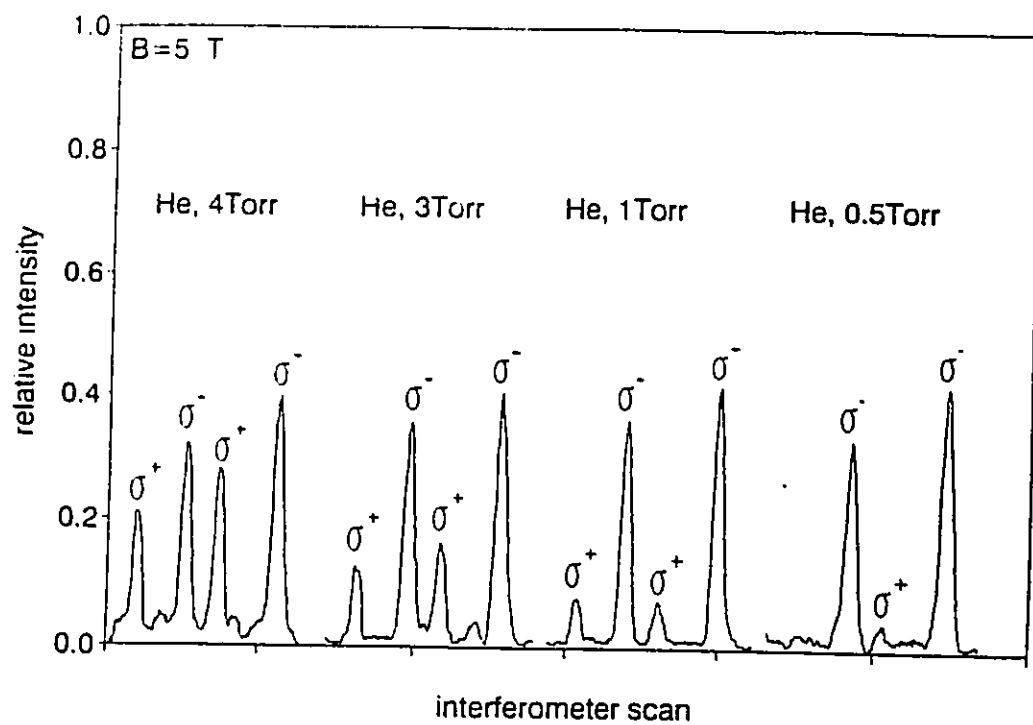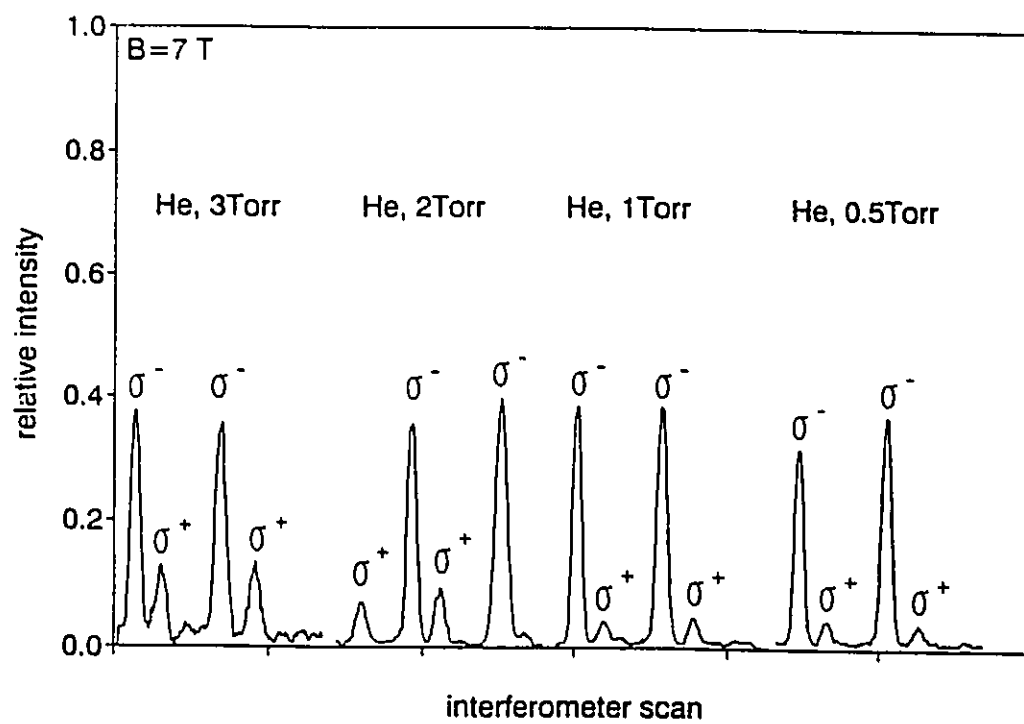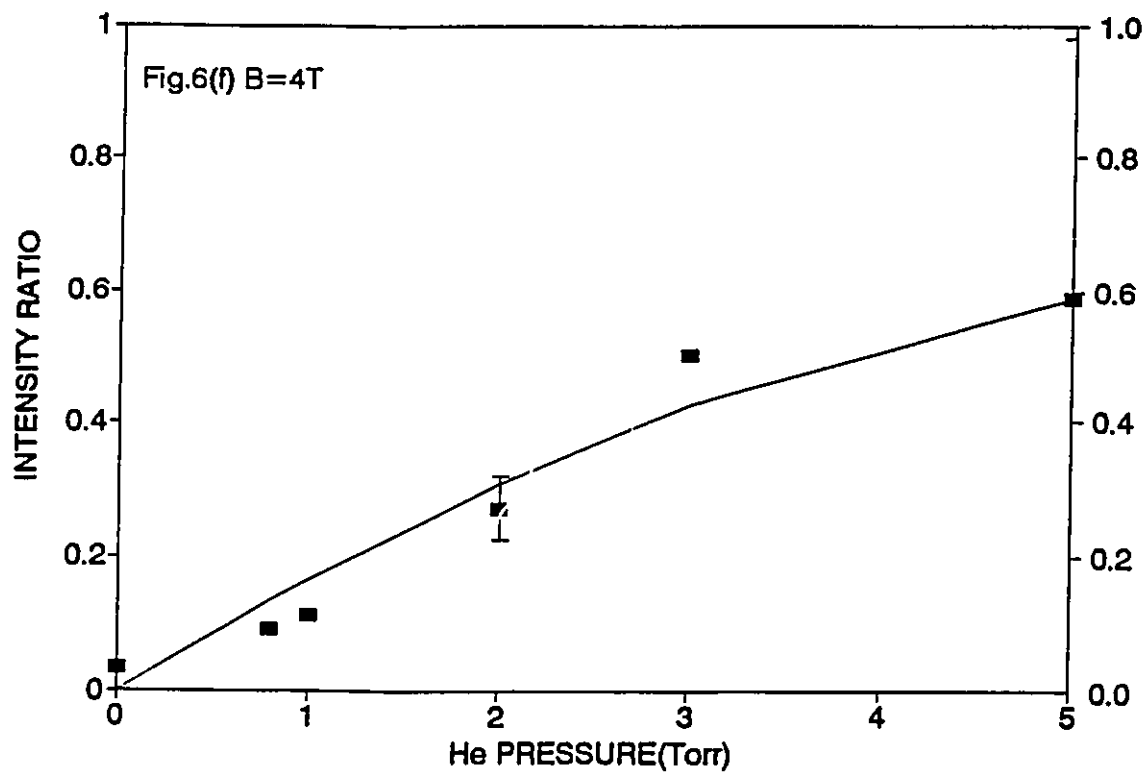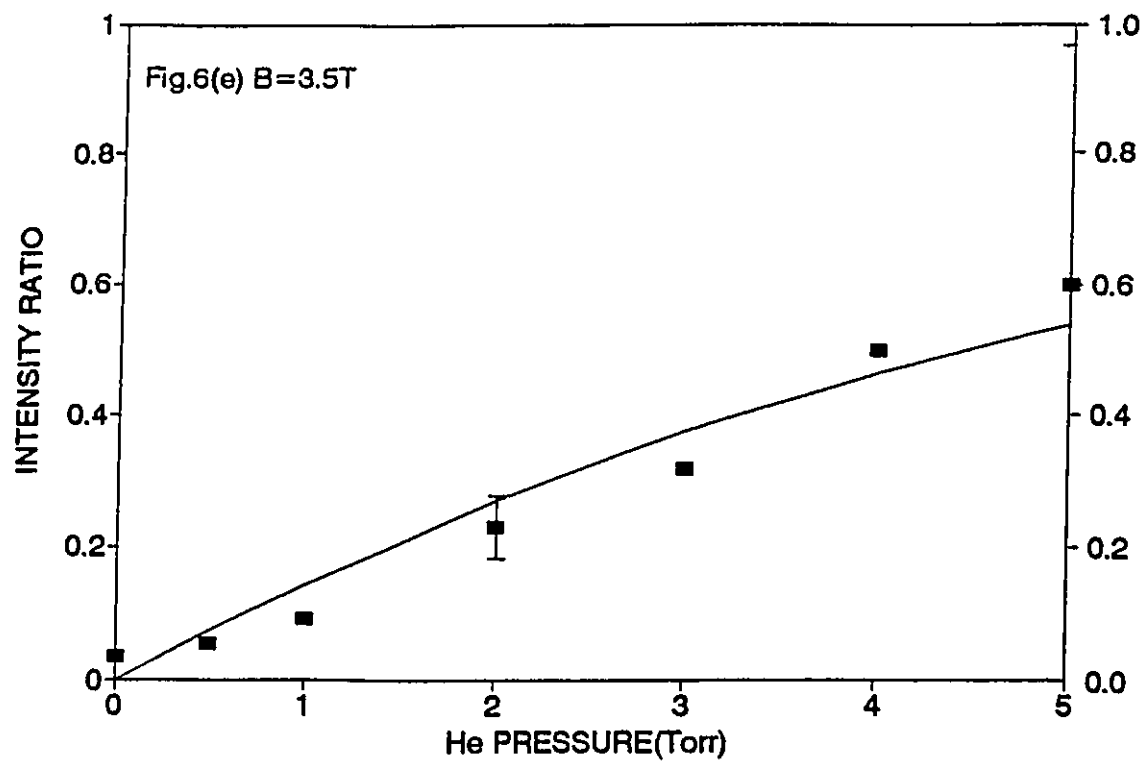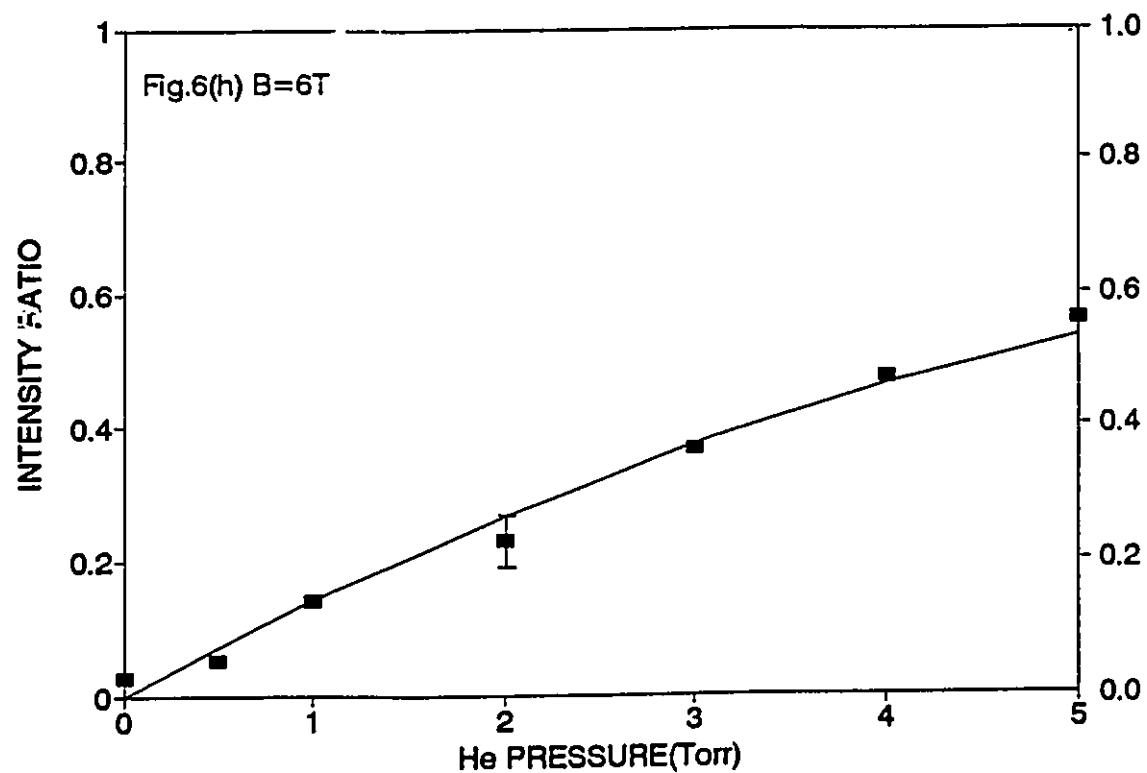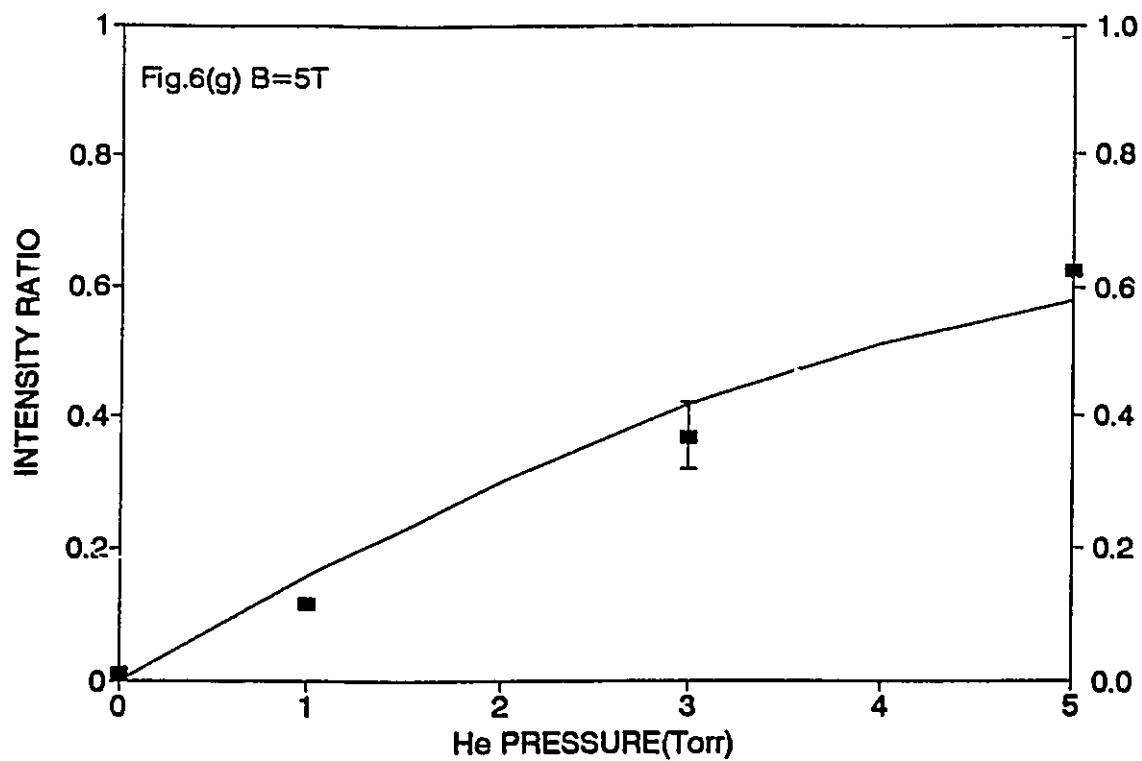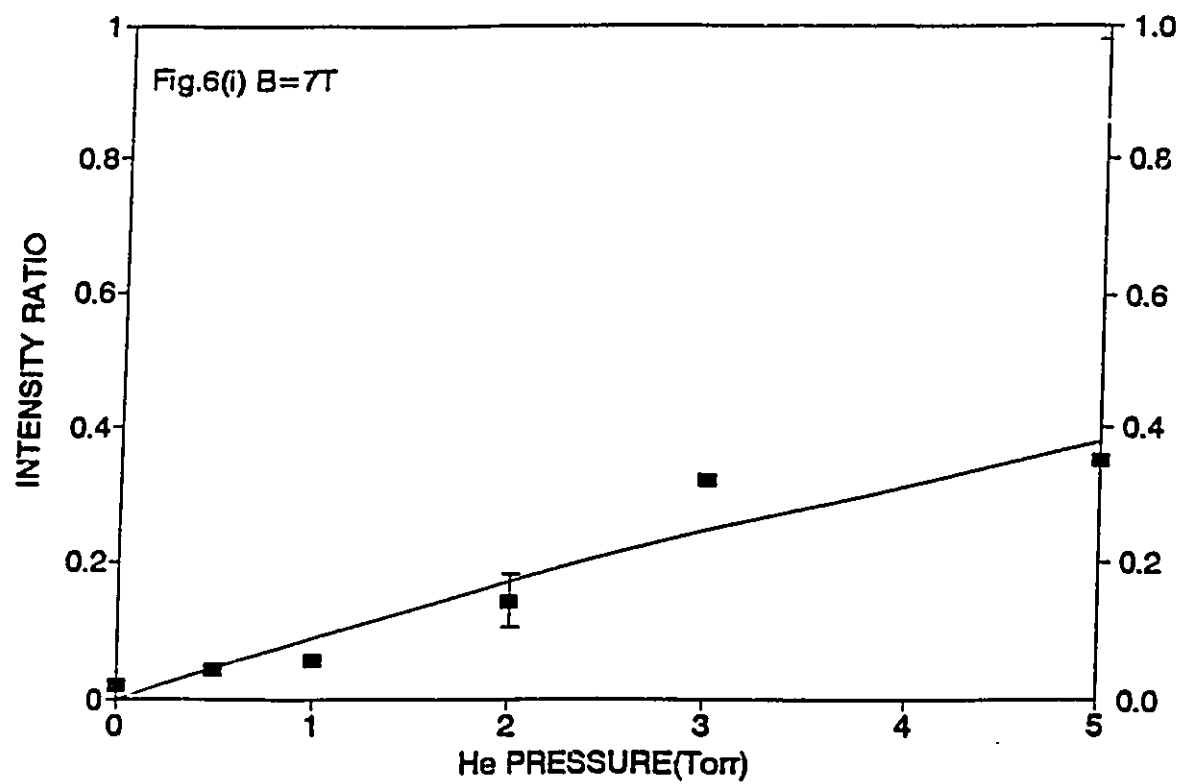
various magnetic field strengths corresponding to those in Fig.5. Since temperatures were held within a narrow range from 307 K to 310 K and were almost uniform in the body of the cell and in the side-arm, an average of 308K was assumed in the calculation. The solid curves represent best fits of eq.(IV.1), obtained by using the least-squares method. The time parameters of the laser pulse were measured in order to obtain the parameters used in eq.(IV.1). The pulse half-width Δ was found to be 3.5ns and the delay time defined as the time from the peak of the actual excitation pulse to the counting of fluorescence signals was measured to be $t_0=30\pm5$ns. The electronic jitter was found to be $\delta=15\pm5$ns and the $6^2P_{1/2}$ life time was $\tau=34$ns. The best fit to the data is given by
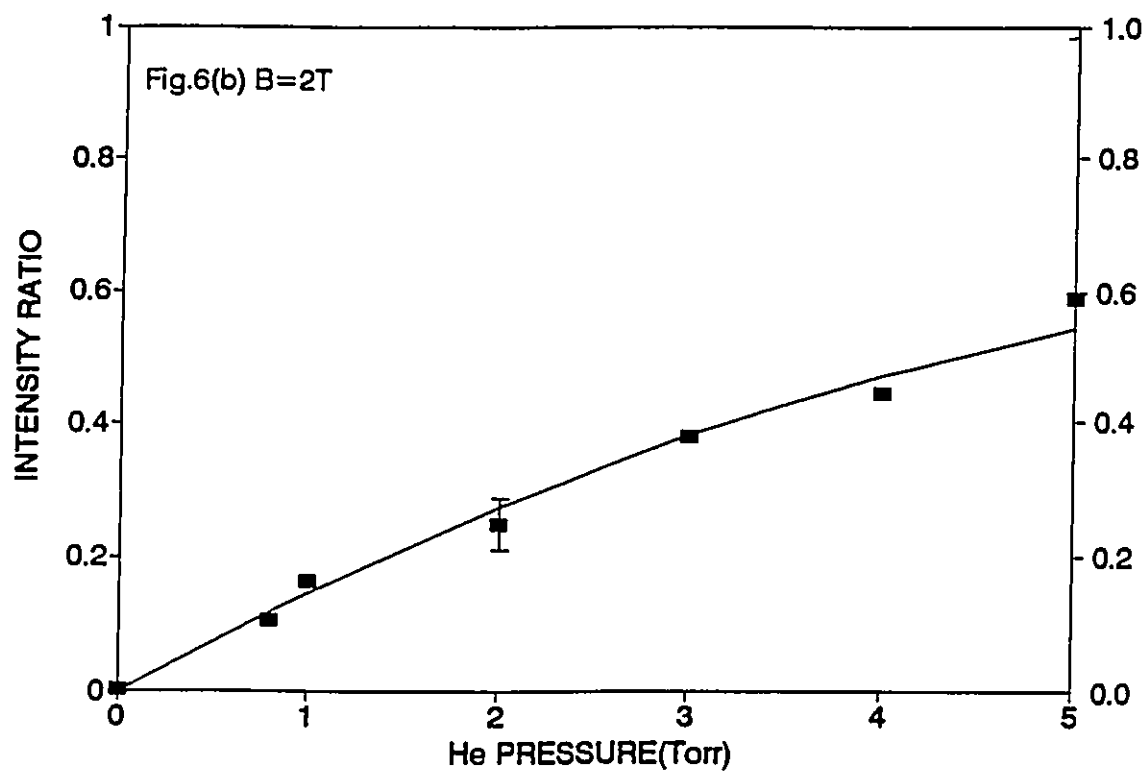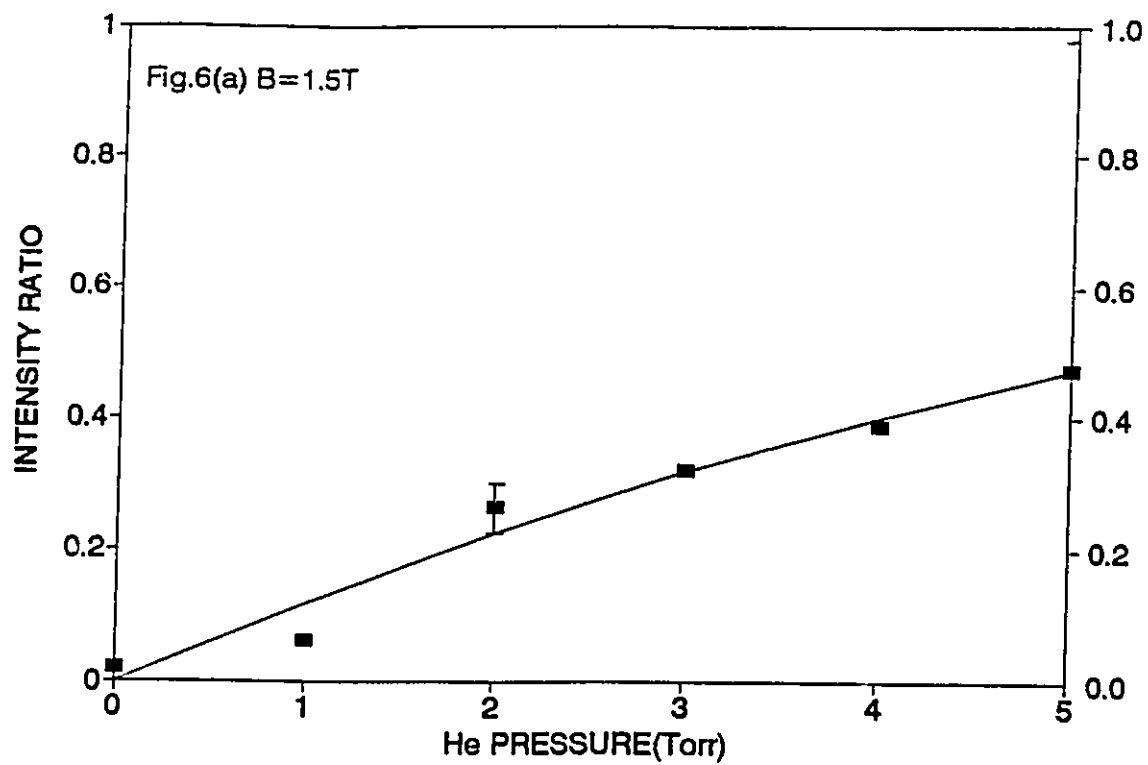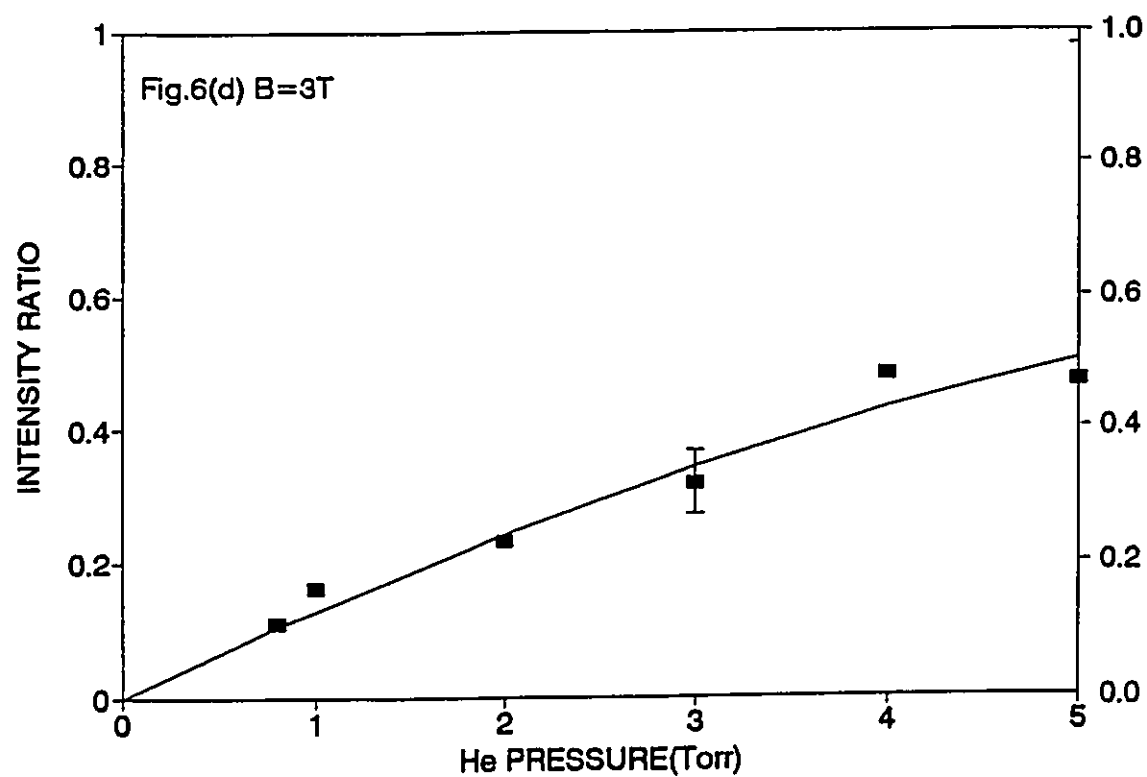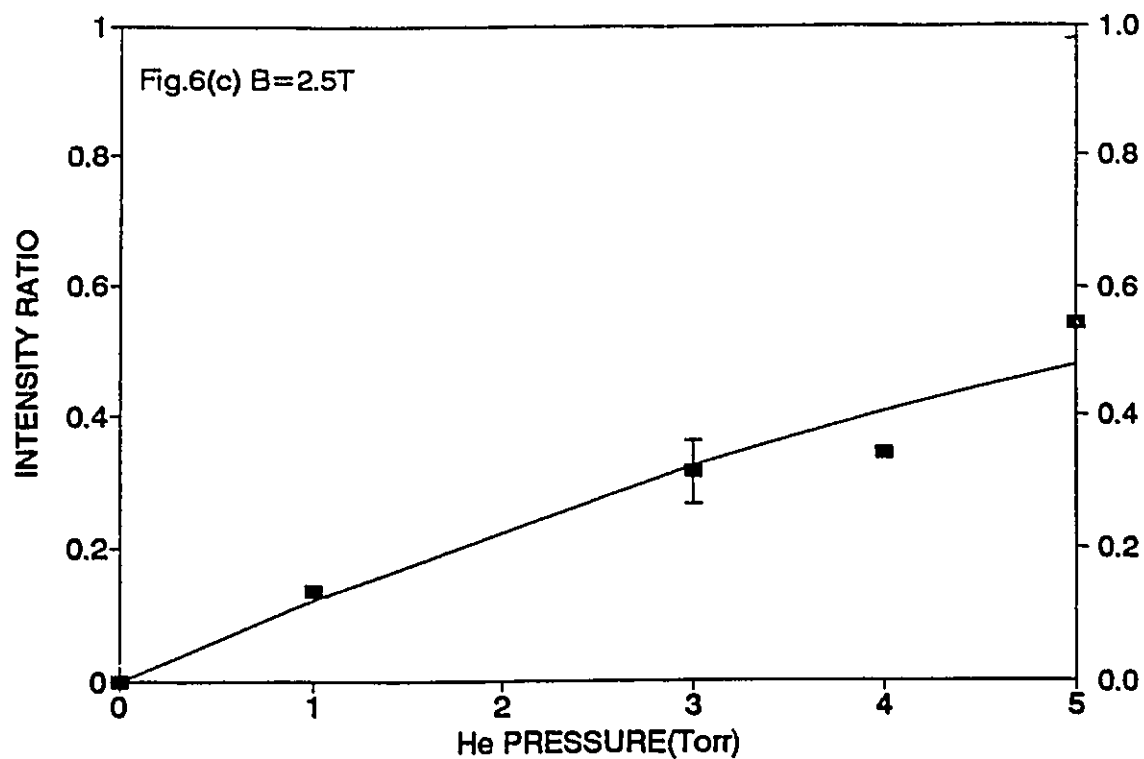
$$\eta=QNv_r\tau(1.76\pm0.18)-(QNv_r\tau)^2(1.1\pm0.03) \tag{IV.3}$$

The errors represent the uncertainties in accurately determining the laser line width and delay time. They are greater than the statistical errors in least-square fitting and will finally yield the systematic error in the cross section.

It is shown in Fig.6 that the fitted curves agree well with the experimental data, which confirms the validity of eq.(II.2.18), except for very large pressures where $Z\tau$ is around 0.4 and the $(Z\tau)^3$ term has to be included in the expression for η. To consider the uncertainty in eq.(IV.3), it is not necessary to include the $(Z\tau)^3$ term in the fitting procedure, because the deviations of the experimental data

49

from the fitted curve are within the error bars.

The cross sections Q, which were thus determined by fitting eq.(IV.3) at nine values of B ranging from 1.5 T to 7 T, are plotted in Fig.7 against the magnetic field strength, together with the previous data (Guiry and Krause 1975) ranging from 0 to 0.98 T. The plot shows a general increase of the cross section with the field strength which confirms the enhancement effect of the magnetic field.

It is apparent in Fig.7, that there are two ranges of variation of the cross section Q with the magnetic field, separated by a 'turning point' at $B_{TURN}=0.76T$. This value when substituted in eq.(II.1.38), gave the hard-core collision radius $R_0 = 2.8a_0$, where a_0 is the Bohr radius. This value is very close to the previously calculated result, $R_0 = 3.2\ a_0$ (Baylis 1977). $R_0 = 2.8\ a_0$ was used in eq.(II.1.37) to obtain $\lambda = 3.143\times10^3$ which, when substituted in eq.(II.1.35) gave $C'_1 = 9.67$ a.u. These values, resulting from a one-point fit of eq.(II.1.40) to the experimental data, make it possible to represent the variation of Q with the magnetic field B.

$$Q = 10.7 + 14.6B^2 \text{ a.u.} = 3 + 4.1B^2(\text{\AA}^2) \quad (B < 0.76T) \qquad \text{(IV.4)}$$

$$= 10.7 + 9.67B^{0.45} \text{ a.u.} = 3 + 2.71^{0.45}(\text{\AA}^2) \quad (B \geq 0.76T) \quad \text{(IV.5)}$$

Equations (IV.4) and (IV.5) are also plotted in Fig.7 in juxtaposition with the experimental data and it may be seen that there is very good agreement between the theoretical and experimental data in the range $0 < B < 5T$. At $B = 5T$ the experimental measurements suggest a peak in the cross section

50

Figure 7. A plot of the Zeeman mixing cross section Q against magnetic-field strength. The filled square points represent this experimental data and the blank square points represent the previous result (Guiry and Krause 1975). The solid curve are the results of the theoretical calculation. The error bars represent the systematic errors.
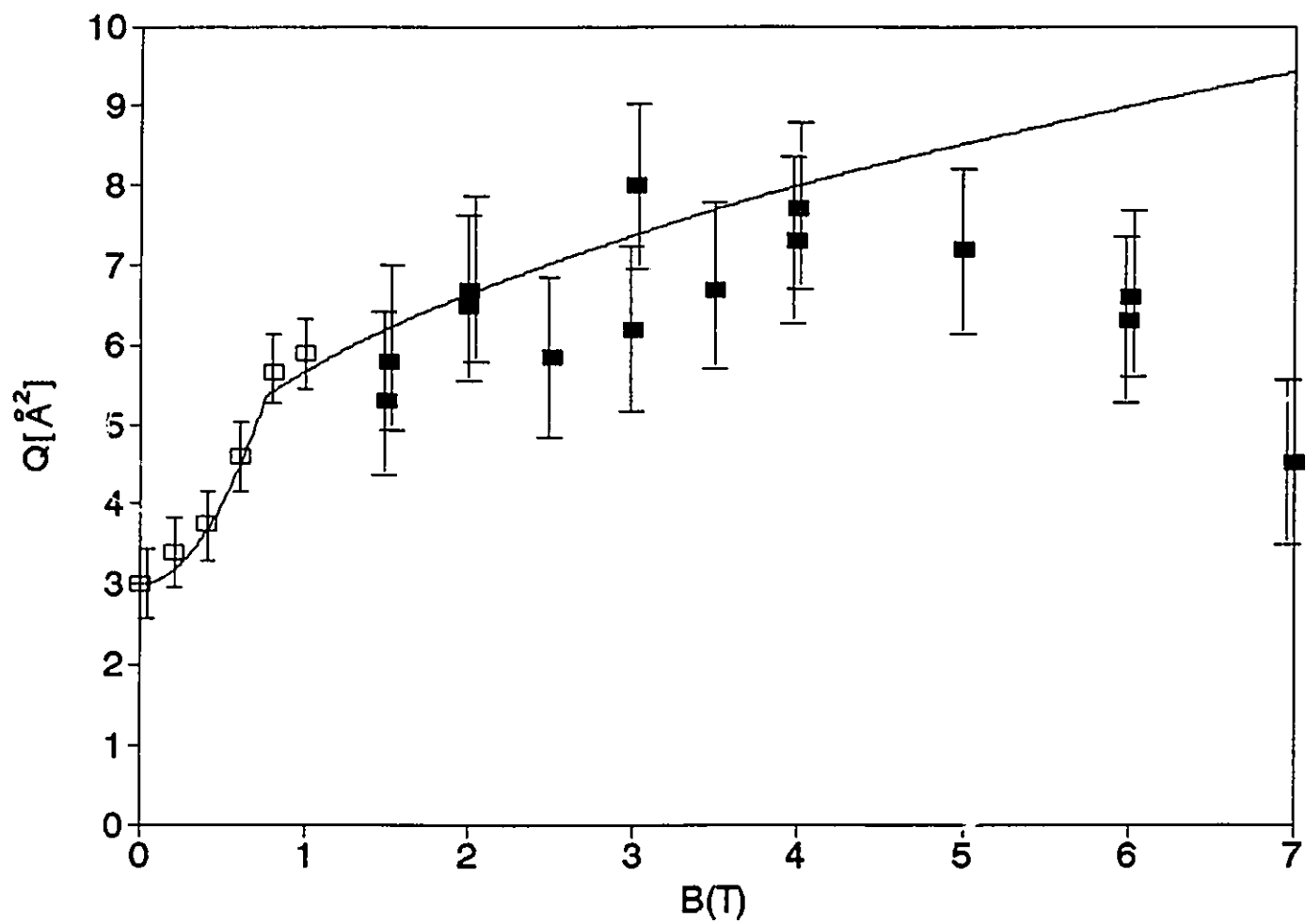
followed by a slight decline of the cross section at B > 5T, though the calculated curve indicates a continued increase. It is intended to pursue the calculation further and examine the possible mechanisms that could account for the decrease of the Zeeman mixing cross section at high magnetic fields.

The experimental and theoretical data also provide information on the Cs + He interaction. The coefficient C_n in eq.(II.1.20) was obtained using $\lambda = 3.14 \times 10^3$ in eq.(II.1.24), which yielded $C_n = 1.23 \times 10^2$. Accordingly, the repulsive interaction potential involved in the Cs + He collision has the form

$$V(R) = 1.23 \times 10^2 R^{-5.46} \text{ a.u.} \tag{IV.6}$$

The form of this potential differs from an earlier version $V(R) = 1.12 \times 10^3 R^{-5.46}$ a.u., which was obtained from a fit to the experimental data of Guiry and Krause (1975) but without including the residual cross section Q_0 in the theoretical analysis. The Q_0 term resulted from the inclusion of second-order perturbation which had not been included previously and which, presumably, produced a more accurate result. Our result reveals a "soft" repulsive potential and therefore gives a smaller hard-core radius.

It should also be pointed out that the Zeeman mixing cross section Q is directly related to the cross section $\sigma_{1/2}^{(1)}$ for the relaxation of the bulk dipole moment (orientation)

52

associated with the $^2P_{1/2,-1/2}$ population, where

$$\sigma_{1/2}^{(1)} = 2Q \qquad \qquad \text{(IV.7)}$$

Accordingly, the results of this work are equally useful for studies of collisional relaxation of atomic multipole moments, which results from collisional mixing among Zeeman states.

V   CONCLUSIONS

This thesis describes an experimental and theoretical
investigation of the magnetic field dependence of the Zeeman
mixing cross section for collisions of oriented Cs $6^2P_{1/2}$ atoms
with ground-state He atoms. The collisional interaction of Cs
atoms with He atoms at thermal energies near room temperature
has been studied by selectively exciting the Cs $6^2P_{1/2,-1/2}$
Zeeman state by laser radiation and measuring the relative
intensities of the direct and sensitized fluorescence
components. The two components were resolved with a stabilized
Fabry-Perot interferometer and their intensities were recorded
by a photomultiplier. A superconducting magnet was used to
generate fields up to 7 T and the Zeeman cross sections were
measured at nine magnetic-field strengths ranging from 1.5 T
to 7 T. The experimentally determined field-dependence of the
cross section is shown in Fig.7, together with the
theoretically predicted dependence calculated using time-
dependent perturbation theory. Both the experimental and
theoretical results show the enhancement of the mixing cross
section by the magnetic field and are in very good agreement
up to B=5 T. The experimentally found decline of the cross
section at fields stronger than 5 T is not predicted by the
calculations contained in this thesis but an extension of the
calculation is planned for the future.

APPENDIX A

Calculation of the energy levels of the Cs 6^2P

states in the presence of a magnetic field

The time-dependent perturbation calculation in section II.1 of this thesis was based on the following assumptions: (a) the field B is sufficiently weak that Zeeman splittings (~ μ_0B) are small compared to the energy uncertainty ~$\hbar/\tau_c$, where τ_c is the collision time. Accordingly: $\mu_0B\tau_c \ll \hbar$ [see eq.(II.1.8)]

(b) B is weak enough that the $P_{1/2}$-$P_{3/2}$ virtual mixing which it induces, can be calculated by perturbation theory: $\mu_0B \ll \Delta E$ [see eq.(II.1.8)]

(c) B is strong enough to decouple the nuclear spin I from the electronic angular momentum $J=L+S$.

According to Table 1., conditions (a) and (b) were satisfied as the Zeeman splitting is less than 7 cm^{-1} even at B= 7 T. To justify condition (c), a numerical calculation was performed of the energy eigenvalues in an external magnetic field, assuming all possible angular momentum couplings in the Cs atom. The Hamiltonian is:

$$H=H_0+H_{HFS} \tag{A.1}$$

where

$$H_0=-\frac{\nabla^2}{2M}+V_{eff.}(r) \tag{A.2}$$

55

is the uncoupled Hamiltonian of an electron in an effective potential $V_{eff.}(r)$ which becomes Coulombic at large r. H_{HFS} includes couplings among the angular momenta L, S, I, the orbital, electron spin and nuclear spin angular momenta respectively, as well as the couplings of the corresponding magnetic moments to the magnetic field

$$H_{HFS} = A_J \mathbf{I \cdot J} + \frac{B_J}{2I(2I-1)J(2J-1)} \times [3(\mathbf{I \cdot J})^2 + \frac{3}{2}(\mathbf{I \cdot J}) - I(I+1)J(J+1)]$$

$$+ (g_L \mu_B \mathbf{L} + g_s \mu_B \mathbf{S}) \cdot \mathbf{B} - g_I \mu_n \mathbf{I \cdot B} + \xi(r) \mathbf{L \cdot S} \qquad (A.3)$$

where A_J and B_J are two coupling constants for the interaction between the nucleus and the electrons . The term containing A_J represents the magnetic dipole interaction between I and J while the term containing B_J represents the electric quadrupole interaction between I and J. $\xi(r)$ is the L-S coupling coefficient.

In order to calculate the energy eigenvalues of the above Hamiltonian, $|LM_L SM_S IM_I\rangle$, the eigenfunction of H_0, was chosen as the basis set. The matrix elements of the Hamiltonian in this basis could be calculated and expressed in terms of the quantum numbers L, M_L, S, M_S, I, M_I. The constants in the expression were found to be the following, all in atomic units (a.u.) except where otherwise indicated:

$g_L = 1$

$g_S = 2$

$g_I = 0.000398854$ [E.Arimondo et al]

$\mu_B = 2.127176 \times 10^{-6}$

$\mu_n = 1.158495 \times 10^{-9}$

$A_{J=1/2} = 4.4363860 \times 10^{-14}$

$B_{J=1/2} = 0$

$A_{J=3/2} = 7.6508280 \times 10^{-15}$

$B_{J=3/2} = -5.7753569 \times 10^{-17}$

The values A_J and B_J were taken from Arimondo et al.(1977)

$\xi(r)$ was determined from the fine structure splitting

$\Delta E(6^2P_{1/2} \rightarrow 6^2P_{3/2}) = 551 \text{ cm}^{-1}$, and from eq.(A.3) to have the value:

$\xi(r) = 2\Delta E/3 = 1.2830628 \times 10^{-3}$ (A.4)

The energy eigenvalues of the Hamiltonian H can be obtained by diagonalizing the matrix of the Hamiltonian in the above basis. The energy eigenvalues which were calculated for various values of the magnetic field B are listed in Table 2. A partial plot against B containing six out of the 48 hyperfine Zeeman levels is shown in Fig.8.

The calculation produced the following results:

(1) The precession frequency of the nuclear spin I about the external field B was about 4×10^{-6} a.u. for B=1 T. By comparing it with the frequency of precession of the nuclear spin about the electron total angular momentum J (the hyperfine structure splitting), which is of the order of $10^{-9} - 10^{-8}$, it was concluded that a field strength of not more than 0.1 T was
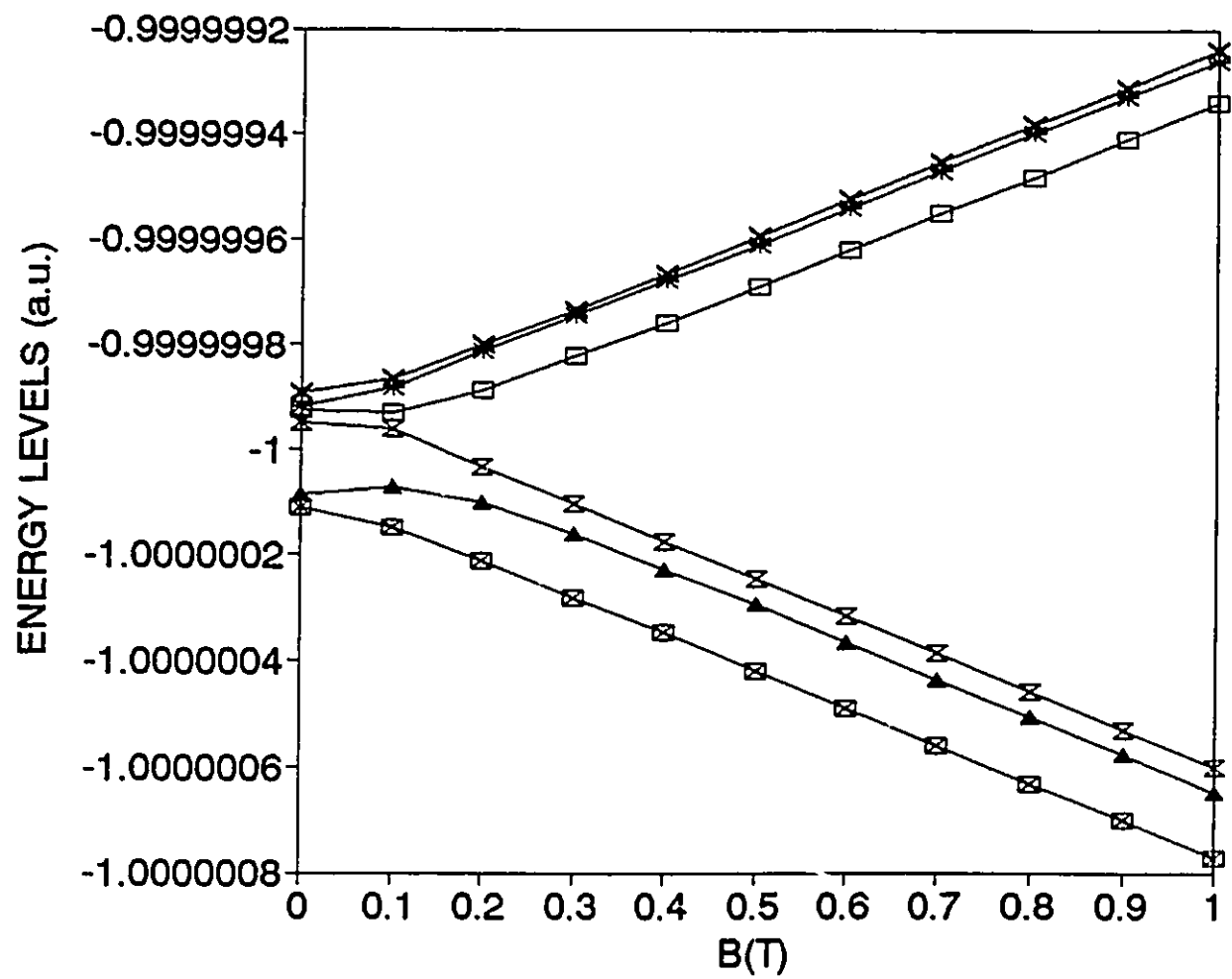
sufficient to decouple the I from J. (see Fig.8)

(2) In the range of $0 < B < 7$ T, the hyperfine structure splittings in the Cs atom in an external magnetic field were very small compared to the fine structure Zeeman splittings. Thus the $P_{1/2}$ Zeeman energy levels never crossed the $P_{3/2}$ levels at any field strength. (see Table 2)

This calculation, accordingly, justifies condition (c) above and indicates that the mixing cross section calculation could be carried out neglecting the hyperfine structure effect.

Table 2. Hyperfine Zeeman Energy Levels of 6^2P Cs atom at various Magnetic-field strengths in the range $0 \leq B \leq 7T$

B(T)	ENERGY LEVEL(a.u.)	B(T)	ENERGY LEVEL(a.u.)
0	0.50000005496703	1	0.50000429450373
0	0.50000004624174	1	0.50000428314833
0	0.50000004409877	1	0.50000427175695
0	0.50000004382382	1	0.50000426033054
0	0.5000000433839	1	0.5000042488696
0	0.50000004015482	1	0.50000423737421
0	0.50000004015481	1	0.50000422584401
0	0.50000003880197	1	0.50000421427819
0	0.50000003822081	1	0.50000146130298
0	0.5000000369221	1	0.50000143575513
0	0.50000003468894	1	0.50000142139612
0	0.50000001701897	1	0.50000141682639
0	0.50000000893071	1	0.50000140725292
0	0.50000000477807	1	0.50000140451318
0	0.50000000253796	1	0.50000139972623
0	0.50000000142279	1	0.50000139881333
0	0.50000000037358	1	0.49999859934122
0	0.50000000027268	1	0.49999859739033
0	0.49999999766652	1	0.49999859468788
0	0.49999997756501	1	0.49999858883559
0	0.4999999750494	1	0.49999858342831
0	0.49999997470381	1	0.49999857367572
0	0.49999997364694	1	0.49999856555895
0	0.499999972054	1	0.49999855190793
0	0.49999996874288	1	0.4999957858059
0	0.49999996779094	1	0.49999577423101
0	0.49999996141508	1	0.49999576268521
0	0.49999994848738	1	0.49999575116702
0	0.49999994798887	1	0.49999573967541
0	0.49999994761811	1	0.49999572820985
0	0.49999994562599	1	0.49999571677021
0	0.4999994526001	1	0.49999570535677
0	-0.99999989249567	1	-0.99999924132473
0	-0.99999991639502	1	-0.99999924317161
0	-0.99999991700623	1	-0.99999924671823
0	-0.99999991735603	1	-0.99999925931877
0	-0.99999992065063	1	-0.99999927912482
0	-0.99999992620765	1	-0.99999930616901
0	-0.99999992696636	1	-0.99999934052638
0	-0.99999992721346	1	-0.99999938233153
0	-0.99999995222772	1	-1.0000006015531
0	-1.0000000868206	1	-1.0000006482377
0	-1.0000000987685	1	-1.0000006872465
0	-1.0000000992282	1	-1.0000007188075
0	-1.0000001005599	1	-1.0000007430554
0	-1.0000001015282	1	-1.000000760065
0	-1.0000001029865	1	-1.0000007698692
0	-1.0000001135644	1	-1.0000007724663

Table 2 (Continue)

B(T)	ENERGY LEVEL(a.u.)	B(T)	ENERGY LEVEL(a.u.)
2	0.50000854885265	3	0.50001280320156
2	0.50000853744322	3	0.5000127917745
2	0.50000852601402	3	0.50001278033294
2	0.50000851456526	3	0.50001276887697
2	0.50000850309705	3	0.50001275740663
2	0.50000849160939	3	0.50001274592192
2	0.50000848010218	3	0.50001273442275
2	0.50000846857519	3	0.50001272290909
2	0.50000287947473	3	0.50000429761144
2	0.50000285389513	3	0.50000427202135
2	0.5000283944446	3	0.50000425754224
2	0.5000283493672	3	0.5000042530536
2	0.50000282530267	3	0.50000424340072
2	0.50000282259859	3	0.50000424070779
2	0.50000281778149	3	0.50000423588131
2	0.50000281688022	3	0.50000423498371
2	0.49999718126212	3	0.49999576316005
2	0.49999717932933	3	0.4999957612329
2	0.4999971765836	3	0.4999957584738
2	0.49999717078531	3	0.49999575269239
2	0.49999716529328	3	0.49999574717394
2	0.49999715562973	3	0.49999573753835
2	0.4999971473903	3	0.4999957292601
2	0.49999713386188	3	0.49999571577046
2	0.49999153145698	3	0.49998727710807
2	0.49999151993701	3	0.49998726560589
2	0.49999150842889	3	0.49998725411011
2	0.4999914969323	3	0.49998724262059
2	0.49999143544698	3	0.49998723113722
2	0.49999147397282	3	0.49998721965995
2	0.4999914625098	3	0.4999872081888
2	0.49999145105801	3	0.49998719672379
2	-0.9999985333531	3	-0.99999782467904
2	-0.99999853411685	3	-0.99999782506343
2	-0.99999853953749	3	-0.99999783113807
2	-0.99999855266177	3	-0.99999784443687
2	-0.99999857272651	3	-0.99999786457585
2	-0.99999859974148	3	-0.99999789155961
2	-0.99999863372681	3	-0.9999979253972 5
2	-0.99999867471497	3	-0.99999796610299
2	-1.0000013106118	3	-1.0000020196719
2	-1.0000013558556	3	-1.0000020644715
2	-1.0000013940483	3	-1.0000021023828
2	-1.0000014252382	3	-1.0000021334259
2	-1.0000014494577	3	-1.0000021576151
2	-1.000001466727	3	-1.0000021749595
2	-1.0000014770558	3	-1.0000021854637
2	-1.0000014804447	3	-1.0000021891282

Table 2 (Continue)

B(T)	ENERGY LEVEL(a.u.)	B(T)	ENERGY LEVEL(a.u.)
4	0.50001705755048	5	0.5000213118994
4	0.50001704611484	5	0.5000213004588
4	0.50001703466732	5	0.50002128900789
4	0.50001702320797	5	0.50002127754668
4	0.50001701173679	5	0.50002126607518
4	0.50001700025379	5	0.5000212545934
4	0.50001698875892	5	0.50002124310129
4	0.50001697725213	5	0.50002123159883
4	0.50000571574043	5	0.50000713386714
4	0.50000569014527	5	0.50000710826909
4	0.5000056756534	5	0.50000709377072
4	0.50000567117312	5	0.5000070892945
4	0.50000566151178	5	0.50000707962885
4	0.50000565882377	5	0.50000707694322
4	0.50000565399307	5	0.50000707211037
4	0.50000565309709	5	0.50000707121518
4	0.49999434505362	5	0.49999292694631
4	0.49999434312905	5	0.49999292502309
4	0.4999943403638	5	0.49999292225455
4	0.49999433459009	5	0.49999291648489
4	0.49999432905947	5	0.49999291094772
4	0.49999431943665	5	0.49999290133165
4	0.49999431114041	5	0.49999289302572
4	0.49999429766856	5	0.49999287956324
4	0.49998302275915	5	0.49997876841023
4	0.49998301126561	5	0.49997875692167
4	0.49998299977578	5	0.49997874543524
4	0.49998298828959	5	0.49997873395088
4	0.49998297680699	5	0.49997872246857
4	0.49998296532796	5	0.49997871098829
4	0.4999829538525	5	0.49997869951006
4	0.49998294238063	5	0.49997868803388
4	-0.99999711582005	5	-0.99999640688614
4	-0.99999711601135	5	-0.9999964069606
4	-0.99999712241827	5	-0.9999964135637
4	-0.99999713580397	5	-0.99999642700597
4	-0.99999715597744	5	-0.99999644719915
4	-0.99999718294133	5	-0.99999647414963
4	-0.9999972167008	5	-0.99999650786074
4	-0.99999725726378	5	-0.99999654833753
4	-1.0000027287334	5	-1.0000034377962
4	-1.0000027733174	5	-1.0000034822253
4	-1.0000028110868	5	-1.0000035199371
4	-1.0000028420526	5	-1.0000035508555
4	-1.0000028662229	5	-1.0000035750133
4	-1.0000028836027	5	-1.0000035924137
4	-1.0000028941947	5	-1.0000036030585
4	-1.0000028979993	5	-1.0000036069479

Table 2 (Continue)

B(T)	ENERGY LEVEL(a.u.)	B(T)	ENERGY LEVEL(a.u.)
6	0.50002556624831	7	0.50002982059723
6	0.50002555480457	7	0.50002980915137
6	0.50002554335154	7	0.50002979769697
6	0.50002553188925	7	0.50002978623404
6	0.5000255204177	7	0.50002977476257
6	0.50002550893688	7	0.50002976328258
6	0.50002549744677	7	0.50002975179403
6	0.50002548594735	7	0.5000297402969
6	0.50000855199338	7	0.50000997011993
6	0.50000852639356	7	0.50000994451895
6	0.50000851189178	7	0.50000993001556
6	0.50000850741749	7	0.50000992554196
6	0.50000849774958	7	0.50000991587299
6	0.50000849506508	7	0.50000991318889
6	0.50000849023111	7	0.50000990835439
6	0.50000848933629	7	0.5000099074597
6	0.49999150883925	7	0.49999009073291
6	0.49999150691678	7	0.49999008881084
6	0.49999150414635	7	0.49999008603933
6	0.49999149837893	7	0.49999008027311
6	0.49999149283802	7	0.49999007473005
6	0.49999148322566	7	0.49999006511968
6	0.49999147491418	7	0.49999005680502
6	0.49999146145688	7	0.4999900433505
6	0.49997451406132	7	0.4999702597124
6	0.49997450257592	7	0.49997024822913
6	0.49997449109159	7	0.49997023674618
6	0.4999744796083	7	0.49997022526352
6	0.49997446812604	7	0.49997021378115
6	0.49997445664478	7	0.49997020229906
6	0.49997444516454	7	0.49997019081726
6	0.49997443368534	7	0.49997017933576
6	-0.9999956979112	7	-0.99999498886314
6	-0.99999569791497	7	-0.9999949889229
6	-0.99999570465331	7	-0.99999499570132
6	-0.99999571812533	7	-0.99999500919776
6	-0.99999573833116	7	-0.99999502941233
6	-0.99999576527201	7	-0.99999505634592
6	-0.99999579895022	7	-0.99999509000023
6	-0.99999583936925	7	-0.99999513037784
6	-1.0000041468603	7	-1.0000048559257
6	-1.0000041912332	7	-1.0000049002393
6	-1.0000042288605	7	-1.0000049378261
6	-1.000004259747	7	-1.0000049686896
6	-1.00000428396	7	-1.0000049928323
6	-1.00000430131	7	-1.0000050102559
6	-1.0000043119901	7	-1.0000050209614
6	-1.0000043159366	7	-1.0000050249488

REFERENCES

Arimondo E, Inguscio M and Violino P 1977 Rev. Mod. Phys., Vol.49, No.1

Baylis W E 1969 J. Chem. Phys. **51** 2665

Baylis W E 1971 Abstracts of VII ICPEAC, Amsterdam, p.677

Baylis W E 1977 Theory of magnetic-field enhancement of disorientation rates for isolated $P_{1/2}$ levels, IX EGAS, Krakow

Baylis W E 1979 in Progress in Atomic Spectroscopy, Part B, W. Hanle and H.Kleinpoppen, eds. (Plenum, NY)

Baylis W E 1993 Private communication.

Berends R.W., Kedzierski W. and Krause L 1988 Phys. Rev. A **37** 68

Gay J C and Schneider W B 1979a Phys. Rev. A **20** 905

Gay J C and Schneider W B 1979b Phys. Rev. A **20** 894

Guiry J and Krause L 1975 Phys. Rev. A **12** 2407

Han X L and Schinn G W 1991 Phys. Rev. A **43** 2661

Kimura M, Kato H, Someda K and Nakamura H 1992 J.Chem. Phys. **96** 7423

Kedzierski W, Middleton R B and Krause L 1991 Phys. Rev. A **43** 143

Link J K 1966 J. Opt. Soc. Amer. **56** 1195

Matsumoto S, Shiozawa, Ishitani Y, Hirabayashi A and Fujimoto T 1991 Phys. Rev. A **44** 4316

Mestdagh J M, Meynadier P, de Pujo P, Sublemontier O, Visticot
J P, Berlande J, Cuvellier J, Gustavsson T, Suits A G, and Lee
Y T 1993 Phys. Rev. A **47** 241

Niefer R J and Atkinson J B 1988 Opt. Commun. **67** 139

Pace P and Atkinson J B 1974 Can.J.Phys. **52** 1635

VITA AUCTORIS

I was born in Shanghai, China on February 24, 1967. After graduating from Shanghai Middle School in Shanghai, I began to study physics at Tsinghua University in Beijing, China and obtained my B.Sc. in June, 1990. After graduation I entered the Institute of Physics at the Chinese Academic of Sciences as a research assistant and remained there until my arrival at the Department of Physics, University of Windsor in September, 1991. I have been awarded a Visa differential fee scholarship and a summer research scholarship in the University of Windsor.